

V-line tensor tomography: numerical results

Gaik Ambartsoumian* Rohit Kumar Mishra† Indrani Zamindar‡

Abstract

This article presents the numerical verification and validation of several inversion algorithms for V-line transforms (VLTs) acting on symmetric 2-tensor fields in the plane. The analysis of these transforms and the theoretical foundation of their inversion methods were studied in a recent work [8]. We demonstrate the efficient recovery of an unknown symmetric 2-tensor field from various combinations of the longitudinal, transverse, and mixed VLTs, their corresponding first moments, and the star VLT. The paper examines the performance of the proposed algorithms in different settings and illustrates the results with numerical simulations on smooth and non-smooth phantoms.

Keywords: Inverse problems, V-line transform, broken ray transform, star transform, tensor tomography, numerical simulations, inversion algorithms, numerical solution of PDEs

Mathematics subject classification 2010: 44A12, 44A60, 44A30, 47G10, 65R10, 65R32

1 Introduction

Various generalizations of the Radon transform, involving integrals over piecewise linear trajectories, have been considered in recent years by different research groups. Some typical examples include operators mapping a scalar function to its integrals along broken rays/lines (also called “V-lines”) or over stars (finite unions of rays emanating from a common vertex). Such integral transforms appear in single scattering optical tomography [17, 20], single scattering X-ray tomography [28, 35], fluorescence imaging [19], Compton camera imaging [12, 13], Compton scattering emission tomography with collimated receivers [29, 34], and gamma ray transmission/emission imaging [31]. A detailed discussion of the history and the state of the art in studies of these generalized Radon transforms, as well as their applications in various imaging modalities can be found in the recent book [3].

From the mathematical point of view, the broken ray/V-line transforms and their generalizations can be split into two distinct groups: those with the vertices of integration submanifolds inside the support of the integrand, and those where the vertices are outside (or on the boundary) of the support. This paper deals with transforms of the first type, and we briefly review below the relevant results on the subject. Several VLTs defined through a rotation invariant family of V-lines were studied in [1, 9, 11, 33], where the authors came up with various inversion formulas of the transforms, as well as implemented and analyzed the performance of the resulting numerical algorithms. VLTs using translation invariant families of V-lines were studied in [4, 18, 22, 27, 28,

*Department of Mathematics, University of Texas at Arlington, Arlington, TX, United States of America. gambarts@uta.edu

†Department of Mathematics, Indian Institute of Technology, Gandhinagar, Gujarat, India. rohit.m@iitgn.ac.in, rohittifr2011@gmail.com

‡Department of Mathematics, Indian Institute of Technology, Gandhinagar, Gujarat, India. indranizamindar@iitgn.ac.in

33]. The obtained results included different inversion formulas, their numerical verification and validation, range description of the transforms, and support theorems. VLTs arising in imaging models using curvilinear detectors (corresponding to V-lines with focused rays) have been analyzed in [27, 28, 33]. Microlocal analysis of VLTs has been discussed in [2, 33]. The study of various properties and the inversion of the star transform has been conducted in [5, 36]. Several extensions of the VLT to three and higher dimensions (the conical Radon transforms) have been studied in [4, 21, 22, 30]. The V-line transform has also been generalized to more general objects, such as vector and tensor fields in \mathbb{R}^2 . In [6], the authors introduced a new set of generalized V-line transforms (longitudinal, transverse, and their first integral moments), studied their properties, and derived various inversion algorithms to recover a vector field in \mathbb{R}^2 from different combinations of those transforms. The numerical verification and validation of the inversion methods proposed in [6] were demonstrated in the follow-up article [7]. Motivated by [1, 6, 9], the authors of [14] studied rotationally invariant V-line transforms of vector fields and came up with two approaches for recovering the unknown vector field supported in a disk.

Another class of integral transforms considered in the literature is concerned with broken rays reflecting from the boundary of an obstacle (sometimes known as a reflector). In [25], the authors studied this problem for scalar fields on a Riemannian surface in the presence of a strictly convex obstacle. Later, that work was extended to symmetric m -tensor fields in a similar setting in [24]. The broken ray transform of two tensors arises from the linearization of the length function of broken rays [25] and can be used in the field of seismic imaging. Notably, in this setting the authors showed that the kernel of the longitudinal transform consists of all potential tensor fields, which is aligned with the theory of straight-line transforms. In a recent work [26], the authors considered a similar setup and proved uniqueness results for the broken ray transform acting on a combination of functions and vector fields on smooth surfaces.

As a natural extension of works [6, 7], we studied the V-line transforms of symmetric 2-tensor fields in \mathbb{R}^2 and discovered multiple interesting results about those operators [8].

In particular, it was shown that the kernel descriptions of the longitudinal and transverse V-line transforms are very different from their counterparts appearing in the theory of straight-line transforms. We obtained exact inversion formulas to reconstruct a symmetric 2-tensor field from various combinations of longitudinal, transverse, and mixed V-line transforms, and their first integral moments. We also derived an inversion formula for the star transform of symmetric 2-tensor fields. In this paper, our aim is to verify and validate all inversion algorithms arising from the theoretical discoveries of [8], and analyze their performance on various phantoms. All our simulations are done in MATLAB. To show the robustness of our numerical algorithms, we have done the reconstructions in the presence of various levels of noise.

The rest of the article is organized as follows. In Section 2, we introduce the integral transforms of interest and the required notations that we use throughout this article. At the end of that section we present two tables (Tables 1, 2), providing a summary of the algorithms studied in the paper and shortcuts to the appropriate sections discussing the reconstructions from particular combinations of the transforms. Section 3 starts with a description of the phantoms used in numerical simulations and explains the details of generating the forward data. A discussion about numerical solutions of certain partial differential equations (PDEs) required in some of our algorithms is presented at the end of that section. All numerical simulations and image reconstructions are demonstrated in Section 4. This section is divided into subsections, each of which focuses on a specific combination of the transforms used for the reconstruction of the tensor fields (for details, see Tables 1, 2). We conclude the article with acknowledgments in Section 5.

2 Definitions and notations

This section is devoted to introducing the notations and definitions used throughout the article. The bold font letters are used to denote vectors and 2-tensors in \mathbb{R}^2 (e.g., \mathbf{x} , \mathbf{u} , \mathbf{v} , \mathbf{f} , etc.), and the regular font letters are used to denote scalars (e.g. x_i , h , f_{ij} , etc). The space of symmetric 2-tensor fields defined in some disc $D \subset \mathbb{R}^2$ is denoted by $S^2(D)$, and the space of twice differentiable, compactly supported tensor fields is denoted by $C_c^2(S^2; D)$. The inner product in $S^2(D)$ is given by

$$\langle \mathbf{f}, \mathbf{g} \rangle = \sum_{i,j=1}^2 f_{ij}g_{ij} = f_{11}g_{11} + 2f_{12}g_{12} + f_{22}g_{22}. \quad (1)$$

Next, we recall various well-known differential operators on scalar functions, vector fields, and tensor fields, which are needed in the upcoming discussions. For a scalar function $\varphi(x_1, x_2)$ and a vector field $\mathbf{f} = (f_1, f_2)$, we use the notations

$$d\varphi = \left(\frac{\partial \varphi}{\partial x_1}, \frac{\partial \varphi}{\partial x_2} \right), \quad d^\perp \varphi = \left(-\frac{\partial \varphi}{\partial x_2}, \frac{\partial \varphi}{\partial x_1} \right), \quad \delta \mathbf{f} = \frac{\partial f_1}{\partial x_1} + \frac{\partial f_2}{\partial x_2}, \quad \delta^\perp \mathbf{f} = \frac{\partial f_2}{\partial x_1} - \frac{\partial f_1}{\partial x_2}. \quad (2)$$

These operators are naturally generalized to higher-order tensor fields in the following way:

$$(d\mathbf{f})_{ij} = \frac{1}{2} \left(\frac{\partial f_i}{\partial x_j} + \frac{\partial f_j}{\partial x_i} \right), \quad \mathbf{f} \text{ is a vector field}, \quad (3)$$

$$(d^\perp \mathbf{f})_{ij} = \frac{1}{2} \left((-1)^j \frac{\partial f_i}{\partial x_{3-j}} + (-1)^i \frac{\partial f_j}{\partial x_{3-i}} \right), \quad \mathbf{f} \text{ is a vector field}, \quad (4)$$

$$(\delta \mathbf{f})_i = \frac{\partial f_{i1}}{\partial x_1} + \frac{\partial f_{i2}}{\partial x_2} = \frac{\partial f_{ij}}{\partial x_j}, \quad \mathbf{f} \text{ is a symmetric 2-tensor field}, \quad (5)$$

$$(\delta^\perp \mathbf{f})_i = -\frac{\partial f_{i1}}{\partial x_2} + \frac{\partial f_{i2}}{\partial x_1} = (-1)^j \frac{\partial f_{ij}}{\partial x_{3-j}}, \quad \mathbf{f} \text{ is a symmetric 2-tensor field}. \quad (6)$$

The directional derivative of a function h in the direction $\mathbf{u} \in \mathbb{S}^1$ is denoted by $D_{\mathbf{u}}$, i.e.

$$D_{\mathbf{u}}h = \mathbf{u} \cdot dh. \quad (7)$$

Remark 1. For a detailed discussion of the operators d , d^\perp , δ , and δ^\perp , we refer to [15, 32].

Consider a pair of fixed linearly independent unit vectors \mathbf{u} and \mathbf{v} . We denote the rays emanating from $\mathbf{x} \in \mathbb{R}^2$ in the directions \mathbf{u} and \mathbf{v} by

$$L_{\mathbf{u}}(\mathbf{x}) = \{\mathbf{x} + t\mathbf{u} : 0 \leq t < \infty\} \quad \text{and} \quad L_{\mathbf{v}}(\mathbf{x}) = \{\mathbf{x} + t\mathbf{v} : 0 \leq t < \infty\}.$$

A V-line with the vertex \mathbf{x} is the union of rays $L_{\mathbf{u}}(\mathbf{x})$ and $L_{\mathbf{v}}(\mathbf{x})$. Since the ray directions are fixed, each V-line can be uniquely identified by the coordinates of its vertex \mathbf{x} .

Now, we are ready to recall the definitions of the transforms of our interest. These operators were introduced in [8], where the authors presented various inversion algorithms to recover a symmetric 2-tensor field from different combinations of the considered transforms.

Definition 1. (a) The *divergent beam transform* $\mathcal{X}_{\mathbf{u}}$ of a function h at $\mathbf{x} \in \mathbb{R}^2$ in the direction $\mathbf{u} \in \mathbb{S}^1$ is defined as:

$$\mathcal{X}_{\mathbf{u}}h(\mathbf{x}) = \int_0^\infty h(\mathbf{x} + t\mathbf{u}) dt. \quad (8)$$

(b) The 1st **moment divergent beam transform** of a function h in the direction $\mathbf{u} \in \mathbb{S}^1$ is defined as follows

$$\mathcal{X}_u^1 h = \int_0^\infty h(\mathbf{x} + t\mathbf{u}) t dt. \quad (9)$$

(c) The **V-line transform** of a function h with branches in the directions $\mathbf{u}, \mathbf{v} \in \mathbb{S}^1$ is defined as follows

$$\mathcal{V}h(\mathbf{x}) = \mathcal{X}_u h(\mathbf{x}) + \mathcal{X}_v h(\mathbf{x}). \quad (10)$$

Definition 2. For two vectors $\mathbf{u} = (u_1, u_2)$ and $\mathbf{v} = (v_1, v_2)$, the tensor product $\mathbf{u} \otimes \mathbf{v}$ is a rank-2 tensor with its ij -th component defined by

$$(\mathbf{u} \otimes \mathbf{v})_{ij} = u_i v_j. \quad (11)$$

The symmetrized tensor product $\mathbf{u} \odot \mathbf{v}$ is then defined as

$$\mathbf{u} \odot \mathbf{v} = \frac{1}{2} (\mathbf{u} \otimes \mathbf{v} + \mathbf{v} \otimes \mathbf{u}). \quad (12)$$

We use the notation \mathbf{u}^2 for the (symmetrized) tensor product of a vector \mathbf{u} with itself, that is,

$$\mathbf{u}^2 = \mathbf{u} \odot \mathbf{u} = \mathbf{u} \otimes \mathbf{u}.$$

Definition 3. Let $\mathbf{f} \in C_c^2(S^2; \mathbb{R}^2)$.

1. The **longitudinal V-line transform** of \mathbf{f} is defined as

$$\mathcal{L}_{u,v} \mathbf{f} = \mathcal{X}_u (\langle \mathbf{f}, \mathbf{u}^2 \rangle) + \mathcal{X}_v (\langle \mathbf{f}, \mathbf{v}^2 \rangle). \quad (13)$$

2. The **transverse V-line transform** of \mathbf{f} is defined as

$$\mathcal{T}_{u,v} \mathbf{f} = \mathcal{X}_u (\langle \mathbf{f}, (\mathbf{u}^\perp)^2 \rangle) + \mathcal{X}_v (\langle \mathbf{f}, (\mathbf{v}^\perp)^2 \rangle). \quad (14)$$

Here $\mathbf{u}^\perp = (u_1, u_2)^\perp = (-u_2, u_1)$ is the normal vector to \mathbf{u} .

3. The **mixed V-line transform** of \mathbf{f} is defined as

$$\mathcal{M}_{u,v} \mathbf{f} = \mathcal{X}_u (\langle \mathbf{f}, \mathbf{u} \odot \mathbf{u}^\perp \rangle) + \mathcal{X}_v (\langle \mathbf{f}, \mathbf{v} \odot \mathbf{v}^\perp \rangle). \quad (15)$$

4. The 1st **moment longitudinal V-line transform** of \mathbf{f} is defined as

$$\mathcal{L}_{u,v}^1 \mathbf{f} = \mathcal{X}_u^1 (\langle \mathbf{f}, \mathbf{u}^2 \rangle) + \mathcal{X}_v^1 (\langle \mathbf{f}, \mathbf{v}^2 \rangle). \quad (16)$$

5. The 1st **moment transverse V-line transform** of \mathbf{f} is defined as

$$\mathcal{T}_{u,v}^1 \mathbf{f} = \mathcal{X}_u^1 (\langle \mathbf{f}, (\mathbf{u}^\perp)^2 \rangle) + \mathcal{X}_v^1 (\langle \mathbf{f}, (\mathbf{v}^\perp)^2 \rangle). \quad (17)$$

6. The 1st **moment mixed V-line transform** of \mathbf{f} is defined as

$$\mathcal{M}_{u,v}^1 \mathbf{f} = \mathcal{X}_u^1 (\langle \mathbf{f}, \mathbf{u} \odot \mathbf{u}^\perp \rangle) + \mathcal{X}_v^1 (\langle \mathbf{f}, \mathbf{v} \odot \mathbf{v}^\perp \rangle). \quad (18)$$

Remark 2. To simplify various calculations, we assume $\mathbf{u} = (u_1, u_2)$ and $\mathbf{v} = (-u_1, u_2)$, that is, the V -lines are symmetric with respect to the y -axis. This choice does not change the analysis of the general case, since the data obtained in one setup of \mathbf{u} and \mathbf{v} can be transformed into the data obtained for the other setup, and vice versa.

Next, we introduce the star transform of symmetric 2-tensor fields. In the upcoming definition, we identify a symmetric 2-tensor $\mathbf{f} = (f_{ij})$ with the vector $\mathbf{f} = (f_{11}, f_{12}, f_{22}) \in \mathbb{R}^3$. Similarly, the tensor products \mathbf{u}^2 and $\mathbf{u} \odot \mathbf{v}$ are identified with the vectors (u_1^2, u_1u_2, u_2^2) and $(u_1v_1, \frac{1}{2}(u_1v_2 + u_2v_1), u_2v_2)$.

Definition 4. Let $\mathbf{f} \in C_c^2(S^2; \mathbb{R}^2)$, and let $\gamma_1, \gamma_2, \dots, \gamma_m$ be distinct unit vectors in \mathbb{R}^2 . The **star transform** of \mathbf{f} is defined as

$$\mathcal{S}\mathbf{f} = \sum_{i=1}^m c_i \mathcal{X}_{\gamma_i} \begin{bmatrix} \mathbf{f} \cdot \gamma_i^2 \\ \mathbf{f} \cdot \gamma_i \odot \gamma_i^\perp \\ \mathbf{f} \cdot (\gamma_i^\perp)^2 \end{bmatrix}, \quad (19)$$

where c_1, c_2, \dots, c_m are non-zero constants in \mathbb{R} .

In our theoretical work [8], we used various combinations of these transforms and derived multiple inversion formulas to recover a symmetric 2-tensor field in \mathbb{R}^2 . All inversion methods and their numerical implementations are discussed in great detail in the upcoming sections, illustrating the effectiveness of the proposed algorithms. The tables below present a summary of these methods, identifying the transform combinations used in each specific method and the section discussing the corresponding reconstruction results. The first table is concerned with the recovery of special kinds of symmetric 2-tensor fields, while the second table deals with the recovery of general symmetric 2-tensor fields.

Form of \mathbf{f}	Combinations of transforms used to recover \mathbf{f}	Sections and Figures
$d^2\varphi$	$\mathcal{L}\mathbf{f}$ or $\mathcal{M}\mathbf{f}$ (formula (28))	4.1.1, Figure 2
$dd^\perp\varphi$	$\mathcal{L}\mathbf{f}$ or $\mathcal{T}\mathbf{f}$ or $\mathcal{M}\mathbf{f}$ (formulas (30) and (31))	4.1.1, Figures 4, 5, 6
$d\mathbf{g}$ PH1	$\mathcal{L}\mathbf{f}$ and $\mathcal{M}\mathbf{f}$ (formulas (32), (33), and (34))	4.1.2, Figures 7, 8, 9, 10
$d\mathbf{g}$ PH2	$\mathcal{L}\mathbf{f}$ and $\mathcal{M}\mathbf{f}$ (formulas (32), (33), and (34))	4.1.2, Figures 11, 12, 13, 14

Table 1: Reconstructions of special kinds of symmetric 2-tensor fields.

Combinations of transforms used to recover \mathbf{f}	Sections and Figures
$\mathcal{L}\mathbf{f}$, $\mathcal{T}\mathbf{f}$, and $\mathcal{M}\mathbf{f}$ ($u_1 = u_2$) (formulas (37), (38), and (39))	4.2, Figures 15, 16
$\mathcal{L}\mathbf{f}$, $\mathcal{T}\mathbf{f}$, and $\mathcal{M}\mathbf{f}$ ($u_1 \neq u_2$) (formulas (40), (41), and (42))	4.2, Figures 17, 18, 19, 20
$\mathcal{L}\mathbf{f}$, $\mathcal{L}^1\mathbf{f}$, and $\mathcal{T}\mathbf{f}$ ($u_1 \neq u_2$) (formulas (44), (43), and (45))	4.3, Figures 21, 22, 23, 24
$\mathcal{L}\mathbf{f}$, $\mathcal{L}^1\mathbf{f}$, and $\mathcal{M}\mathbf{f}$, (formulas (46), (47), and (48))	4.3, Figures 25, 26, 27, 28
$\mathcal{S}\mathbf{f}$ (formula (50))	4.4, Figures 29, 30

Table 2: Full recovery of a general symmetric 2-tensor field.

3 Phantoms, data formation, and numerical solution of PDEs

In this section, we introduce the phantoms used in our numerical experiments and delineate the generation of the forward data. We also discuss the methods used for numerical solution of PDEs appearing in some of the inversion algorithms developed in [8].

3.1 Description of phantoms

The performance of all algorithms will be tested using two phantoms defined on $[-1, 1] \times [-1, 1]$. Since \mathbf{f} is a symmetric 2-tensor field in \mathbb{R}^2 , each phantom has 3 components f_{11} , f_{12} , and f_{22} . In the case of special tensor fields, we use one or two of these functions as scalar or vector potentials of the field.

Phantom 1: \mathbf{f} is a smooth field, and its components f_{11} , f_{12} , f_{22} are different combinations of cutoff functions defined below (see Figure 1). Let $C_r^{(a,b)}$ be the smooth cut-off function, supported in a disk of radius r and center at (a, b) :

$$C_r^{(a,b)}(x, y) = \begin{cases} e^{-r^2/(r^2 - [(x-a)^2 + (y-b)^2])}, & (x-a)^2 + (y-b)^2 < r^2, \\ 0, & (x-a)^2 + (y-b)^2 \geq r^2. \end{cases}$$

$$f_{11}(x, y) = \left[C_{\sqrt{0.05}}^{(0,0)} + C_{\sqrt{0.03}}^{(0.09,0.28)} + C_{\sqrt{0.03}}^{(-0.25,0.15)} + C_{\sqrt{0.03}}^{(-0.22,-0.2)} + C_{\sqrt{0.03}}^{(0.13,-0.27)} + C_{\sqrt{0.03}}^{(0.3,0)} \right] (x, y),$$

$$f_{12}(x, y) = \left[C_{\sqrt{0.1}}^{(0,0)} + C_{\sqrt{0.03}}^{(0.3,0.2)} + C_{\sqrt{0.03}}^{(-0.3,0.2)} \right] (x, y),$$

$$f_{22}(x, y) = \left[C_{\sqrt{0.05}}^{(0,0)}(x, y) + C_{\sqrt{0.03}}^{(0,0.3)} + C_{\sqrt{0.03}}^{(0,-0.3)} + C_{\sqrt{0.03}}^{(-0.3,0)} + C_{\sqrt{0.03}}^{(0.3,0)} \right] (x, y).$$

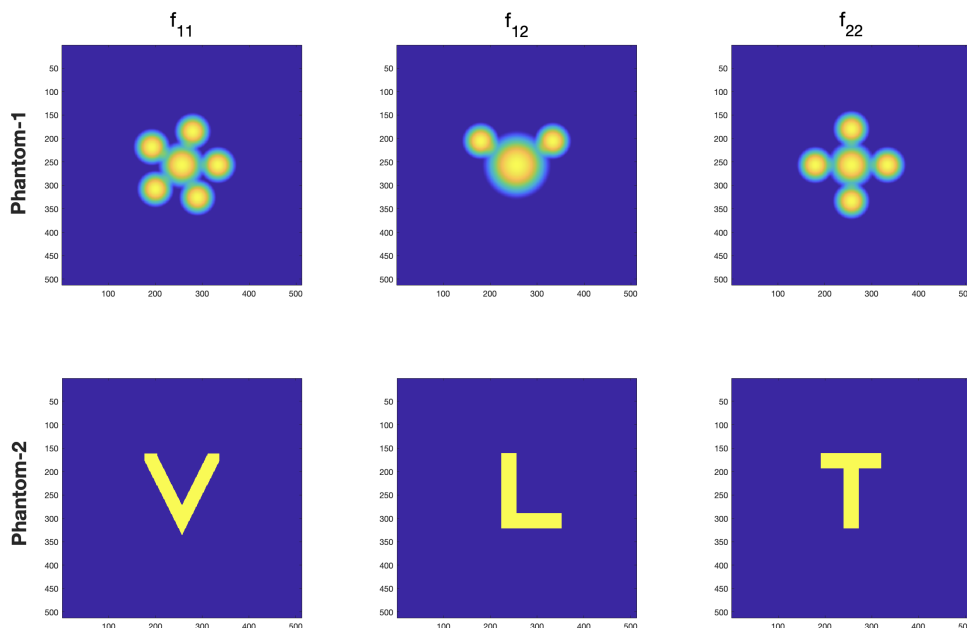


Figure 1: The components of the phantoms considered in numerical reconstructions.

Phantom 2: \mathbf{f} is non-smooth, with its components f_{11} , f_{12} , f_{22} in the shape of the letters “V”, “L”, and “T”, respectively (see Figure 1).

Remark 3.1. It is well known that the numerical inversions of generalized Radon transforms work much better (produce less artifacts) on smooth phantoms than non-smooth ones. As it will be shown below, some of our reconstruction algorithms work extremely well even for the non-smooth phantoms. Therefore, in those cases, we choose to show the reconstructions only for Phantom 2 to save space and avoid repetition.

3.2 Data formation

In the numerical simulations of V-line transforms, we use the unit vectors $\mathbf{u} = (\cos \phi, \sin \phi)$ and $\mathbf{v} = (-\cos \phi, \sin \phi)$, with various choices of the angle $\phi = \pi/3, \pi/4, \text{ or } \pi/6$. In the case of the star transform, we use the setup comprising three branches with polar angles $\phi_1 = 0, \phi_2 = 2\pi/3, \phi_3 = 4\pi/3$, and weights $c_i = 1$ for $i = 1, 2, 3$.

Recall, that all transforms introduced in Definitions 3 and 4 are linear combinations of the divergent beam transform (8) and its first moment (9) of various projections of the unknown tensor field \mathbf{f} . Therefore, to generate the generalized V-line transforms and the star transform of \mathbf{f} , we need a numerical method to compute the divergent beam transform and its first moment of a scalar field. The required algorithm has already been discussed in a recent work [7, Section 3.2], and we briefly present it here for the sake of completeness.

Numerical evaluation of the divergent beam transform and its first moment: Let F be an $n \times n$ pixelized image defined on $[-1, 1] \times [-1, 1]$. Then, the divergent beam transform of F is also of the size $n \times n$, as the discretized set of rays are parametrized by the coordinates of their vertices and are assumed to emanate from the centers of the pixels. Let $\mathbf{x} = (x, y)$ be the vertex, and $\mathbf{u} = (\cos \phi, \sin \phi)$ be the direction of the ray. The first step of the computation is to find the intersections of the ray emanating from \mathbf{x} in the direction \mathbf{u} and the boundaries of square pixels appearing on the path of this ray. Next, we find the product of $F(i, j)$ and the length of the ray inside the pixel (i, j) . By summing up this product over all pixels, one generates the divergent beam transform of F , i.e. $\mathcal{X}_{\mathbf{u}}F(\mathbf{x})$.

To evaluate the first moment of the divergent beam transform of F , we need to consider the product of three quantities $F(i, j)$, the distance from the center of the pixel (i, j) to the vertex \mathbf{x} , and the length of the line segment of the ray inside the pixel (i, j) . Then, by adding this product over all pixels, we get the required $\mathcal{X}_{\mathbf{u}}^1F(\mathbf{x})$.

As discussed above, to generate $\mathcal{L}\mathbf{f}, \mathcal{T}\mathbf{f}$, and $\mathcal{M}\mathbf{f}$ we evaluate the divergent beam transform $\mathcal{X}_{\mathbf{u}}$ of the projections $\langle \mathbf{f}, \mathbf{u}^2 \rangle, \langle \mathbf{f}, (\mathbf{u}^\perp)^2 \rangle, \langle \mathbf{f}, \mathbf{u} \odot \mathbf{u}^\perp \rangle$ and $\mathcal{X}_{\mathbf{v}}$ of $\langle \mathbf{f}, \mathbf{v}^2 \rangle, \langle \mathbf{f}, (\mathbf{v}^\perp)^2 \rangle, \langle \mathbf{f}, \mathbf{v} \odot \mathbf{v}^\perp \rangle$, and combine them according to equations (13) (14), and (15). Similarly, $\mathcal{L}^1\mathbf{f}, \mathcal{T}^1\mathbf{f}$, and $\mathcal{M}^1\mathbf{f}$, are generated by considering $\mathcal{X}_{\mathbf{u}}^1, \mathcal{X}_{\mathbf{v}}^1$ of the appropriate projections and combining them using formulas (16), (17), and (18). Finally, to generate $\mathcal{S}\mathbf{f}$, we consider the divergent beam transform $\mathcal{X}_{\boldsymbol{\gamma}_i}$ of $\mathbf{f} \cdot \boldsymbol{\gamma}_i^2, \mathbf{f} \cdot \boldsymbol{\gamma}_i \odot \boldsymbol{\gamma}_i^\perp, \mathbf{f} \cdot (\boldsymbol{\gamma}_i^\perp)^2$ for $i = 1, 2 \dots m$ and use formula (19) to combine them.

The graphical representations of $\mathcal{L}\mathbf{f}, \mathcal{T}\mathbf{f}$, and $\mathcal{M}\mathbf{f}$ corresponding to Phantoms 1 and Phantom 2 can be found in Figures 17 and 15, respectively. $\mathcal{S}\mathbf{f}$ of Phantom 2 is depicted in Figure 29.

Another operator that is used repeatedly throughout the article is the directional derivative of a scalar function h along \mathbf{u} or \mathbf{v} . Numerically $D_{\mathbf{u}}h$ is computed in the following two steps ($D_{\mathbf{v}}h$ is computed in exactly the same way):

- Calculate the gradient $(\partial_x h, \partial_y h)$ by Matlab function **gradient**.
- Compute $D_{\mathbf{u}}h = u_1 \partial_x h + u_2 \partial_y h$.

Remark 3. In some inversion formulas of [8], one needs to solve initial/boundary value problems for PDEs, which requires an inversion of an $n^2 \times n^2$ matrix. In all such experiments, we use images with a resolution of 160×160 pixels to reduce the computational time. For all other experiments, we use images with a resolution of 512×512 pixels.

3.3 Solving PDEs numerically

As mentioned above in Remark 3, in some cases [8, Theorems 4, 5, and 6] the recovery of the unknown symmetric 2-tensor field is achieved by solving initial/boundary value problems for PDEs. The equations appearing in [8, Theorems 4, 5, and 6] are of the following form:

$$au_{xx} + bu_{yy} = -f, \quad \text{in } \Omega = [-1, 1] \times [-1, 1]. \quad (20)$$

This PDE can be elliptic, parabolic, or hyperbolic in nature, depending on the coefficients a and b . We solve it numerically, with the appropriate initial/boundary conditions discussed below.

Elliptic PDE ($a > 0$ and $b > 0$)

In this case we need to solve numerically the following Dirichlet boundary value problem.

$$\begin{cases} au_{xx} + bu_{yy} = -f & \text{in } \Omega = [-1, 1] \times [-1, 1], \\ u = g & \text{on } \partial\Omega. \end{cases} \quad (21)$$

Dividing Ω into $N \times N$ uniform pixels with the pixel size $h \times h$, we use the central difference approximation to write the second-order derivatives at an interior grid point (x_i, y_j) as:

$$\frac{\partial^2 u}{\partial x^2}(x_i, y_j) = \frac{u_{i+1,j} - 2u_{i,j} + u_{i-1,j}}{h^2}, \quad \frac{\partial^2 u}{\partial y^2}(x_i, y_j) = \frac{u_{i,j+1} - 2u_{i,j} + u_{i,j-1}}{h^2}, \quad (22)$$

where $u_{i,j} = u(x_i, y_j)$. Then the differential operator in equation (21) can be approximated at (x_i, y_j) as follows:

$$[au_{xx} + bu_{yy}](x_i, y_j) = \frac{au_{i-1,j} - 2(a+b)u_{i,j} + au_{i+1,j} + bu_{i,j-1} + bu_{i,j+1}}{h^2}.$$

Thus, the finite difference version of the partial differential equation at the interior points is given by

$$-\frac{au_{i-1,j} - 2(a+b)u_{i,j} + au_{i+1,j} + bu_{i,j-1} + bu_{i,j+1}}{h^2} = f_{i,j}. \quad (23)$$

By defining the index map $(i, j) \rightarrow k = (N-2)(i-2) + (j-1)$ for $2 \leq i, j \leq N-1$, we arrange the interior $(N-2) \times (N-2)$ grid points in one row using a single index $k = 1$ to $(N-2)^2$ and use notations $u_k = u_{i(k),j(k)}$ and $f_k = f_{i(k),j(k)}$. With this choice of indexing, equation (23) takes the following form:

$$AU = F, \quad (24)$$

where $U = (u_k)_{1 \leq k \leq (N-2)^2}$ and A is an $(N-2)^2 \times (N-2)^2$ matrix that has block tridiagonal structure given by

$$A = \begin{pmatrix} B & C & 0 & \dots & 0 & 0 & 0 \\ C & B & C & \dots & 0 & 0 & 0 \\ \vdots & \vdots & \vdots & \ddots & \vdots & \vdots & \vdots \\ 0 & 0 & 0 & \dots & C & B & C \\ 0 & 0 & 0 & \dots & 0 & C & B \end{pmatrix} \quad \text{with} \quad C = -bI_{(N-2) \times (N-2)},$$

$$B = \begin{pmatrix} 2(a+b) & -a & 0 & \dots & 0 & 0 & 0 \\ -a & 2(a+b) & -a & \dots & 0 & 0 & 0 \\ \vdots & \vdots & \vdots & \ddots & \vdots & \vdots & \vdots \\ 0 & 0 & 0 & \dots & -a & 2(a+b) & -a \\ 0 & 0 & 0 & \dots & 0 & -a & 2(a+b) \end{pmatrix}_{(N-2) \times (N-2)},$$

and $F = h^2(\tilde{f}_k)_{1 \leq k \leq (N-2)^2}$. Here \tilde{f} represents the modified source term, which satisfies $\tilde{f}_{i,j} = f_{i,j}$ for $3 \leq i, j \leq N-2$, and involves the boundary terms (i.e. the given data $g(i, j)$) for other indices. More specifically, we have

$$\begin{aligned} \tilde{f}_{2,2} &= f_{2,2} + \frac{1}{h^2}(ag_{1,2} + bg_{2,1}), & \tilde{f}_{N-1,2} &= f_{N-1,2} + \frac{1}{h^2}(ag_{N,2} + bg_{N-1,1}), \\ \tilde{f}_{2,j} &= f_{2,j} + \frac{a}{h^2}g_{1,j}, \quad \text{for } 3 \leq j \leq N-2, & \tilde{f}_{N-1,j} &= f_{N-1,j} + \frac{a}{h^2}g_{N,j}, \quad \text{for } 3 \leq j \leq N-2, \\ \tilde{f}_{i,2} &= f_{i,2} + \frac{b}{h^2}g_{i,1}, \quad \text{for } 3 \leq i \leq N-2, & \tilde{f}_{i,N-1} &= f_{i,N-1} + \frac{b}{h^2}g_{i,N}, \quad \text{for } 3 \leq i \leq N-2, \\ \tilde{f}_{2,N-1} &= f_{2,N-1} + \frac{1}{h^2}(ag_{1,N-1} + bg_{2,N}), & \tilde{f}_{N-1,N-1} &= f_{N-1,N-1} + \frac{1}{h^2}(ag_{N,N-1} + bg_{N-1,N}). \end{aligned}$$

Finally, we solve the system of linear equations $AU = F$ to get U as a numerical solution u of the required boundary value problem (21) in the case when $a > 0$ and $b > 0$.

Parabolic PDE ($a = 0$ or $b = 0$)

For $b = 0$, the PDE (20) reduces to

$$u_{xx} = -f/a. \tag{25}$$

This equation is solved by repeated integration along $e_1 = (1, 0)$.

More specifically, we apply the divergent beam transform \mathcal{X}_{e_1} twice to equation (25) to obtain u .

The case $a = 0$ is treated analogously, by integrating twice in the direction $e_2 = (0, 1)$ to get u .

Hyperbolic PDE (a and b are of opposite signs)

Let us consider the case when $a > 0$ and $b < 0$ (the other case is analogous). For $b = -\tilde{b}$, where $\tilde{b} > 0$, we get the following initial value problem from (20) (see the discussion on [8, Page 10]):

$$\begin{cases} au_{xx} - \tilde{b}u_{yy} = -f & \text{in } \Omega = [-1, 1] \times [-1, 1], \\ u(-1, y) = g, \\ u_x(-1, y) = \tilde{g}. \end{cases} \tag{26}$$

Dividing Ω into $N \times M$ uniform pixels with the pixel size $h \times k$, we use the forward difference approximation for the first-order derivative at the left boundary and the central difference approximation for the second-order derivatives at an interior grid point (x_i, y_j) .

$$\begin{aligned} \frac{\partial u}{\partial x}(x_i, y_j) &= \frac{u_{i+1,j} - u_{i,j}}{h}, & \frac{\partial^2 u}{\partial x^2}(x_i, y_j) &= \frac{u_{i+1,j} - 2u_{i,j} + u_{i-1,j}}{h^2}, \\ \frac{\partial^2 u}{\partial y^2}(x_i, y_j) &= \frac{u_{i,j+1} - 2u_{i,j} + u_{i,j-1}}{k^2}, & \text{where } u_{i,j} &= u(x_i, y_j). \end{aligned}$$

The finite difference version of the hyperbolic PDE is given by

$$\begin{cases} u_{i+1,j} = 2u_{i,j} - u_{i-1,j} + \lambda(u_{i,j+1} - 2u_{i,j} + u_{i,j-1}) - \frac{h^2}{a} f_{i,j}, & 2 \leq i, j \leq (N-1) \\ u_{1,j} = g_{1,j} & 1 \leq j \leq N \\ u_{2,j} = u_{1,j} + h\tilde{g}_{1,j}, & 1 \leq j \leq N \end{cases} \quad (27)$$

where $\lambda = \frac{\tilde{b} h^2}{a k^2}$.

Relation (27) provides a method for iterative solution of the initial value problem (26).

Remark 4. *The stability of the finite difference method discussed above (for the hyperbolic case) depends on the proper balance between the step sizes h and k , given by the Courant-Friedrichs-Lewy (CFL) condition. The CFL condition ensures that the numerical domain of dependence contains the analytical domain of dependence for a given initial condition. In our setting, this condition can be written as:*

$$C \doteq \sqrt{\lambda} \leq 1.$$

The constant C is often called the Courant number. For a more detailed discussion on the CFL condition, please refer to [16, Section 2.2.3]

Remark 5. *Note that all integral transforms (the forward data) are numerically computed on grids with $h = k$. However, for a stable reconstruction using hyperbolic PDEs, in some cases we need to take $h \neq k$. To address this issue we use interpolation to generate the data on a finer grid of size $4N \times N$, that is $k = 4h$, and use this data to solve the given hyperbolic equation in a stable way with the Courant number $C = 1/4$.*

4 Numerical Implementation

In this section, we present the results of the numerical implementation of the inversion algorithms proposed in [8] for the transforms introduced in Section 2. We divide our presentation into subsections, each of which deals with either a particular type of tensor field or a particular combination of transforms used for reconstruction. Each subsection starts with a brief review of the theoretical result implemented there. Below is a summary of the results discussed in this section.

1. Special tensor fields (here φ is a function, and g is a vector field)

- (i) The tensor field $\mathbf{f} = d^2\varphi$ is recovered from either $\mathcal{L}\mathbf{f}$ or $\mathcal{M}\mathbf{f}$.
- (ii) The tensor field $\mathbf{f} = (d^\perp)^2\varphi$ is recovered from either $\mathcal{T}\mathbf{f}$ or $\mathcal{M}\mathbf{f}$.

- (iii) The tensor field $\mathbf{f} = \text{dd}^\perp\varphi$ is recovered from either $\mathcal{L}\mathbf{f}$, or $\mathcal{T}\mathbf{f}$, or $\mathcal{M}\mathbf{f}$.
 - (iv) The tensor field $\mathbf{f} = \text{d}\mathbf{g}$ is recovered from the combination of $\mathcal{L}\mathbf{f}$ and $\mathcal{M}\mathbf{f}$.
 - (v) The tensor field $\mathbf{f} = \text{d}^\perp\mathbf{g}$ is recovered from the combination of $\mathcal{T}\mathbf{f}$ and $\mathcal{M}\mathbf{f}$.
2. \mathbf{f} is recovered from the combination of $\mathcal{L}\mathbf{f}$, $\mathcal{T}\mathbf{f}$ and $\mathcal{M}\mathbf{f}$.
 3. When $u_1 \neq u_2$, \mathbf{f} is recovered from any of the following combinations
 - (a) $\mathcal{L}\mathbf{f}$, $\mathcal{L}^1\mathbf{f}$ and $\mathcal{T}\mathbf{f}$,
 - (b) $\mathcal{T}\mathbf{f}$, $\mathcal{T}^1\mathbf{f}$ and $\mathcal{L}\mathbf{f}$,
 - (c) $\mathcal{M}\mathbf{f}$, $\mathcal{M}^1\mathbf{f}$ and $\mathcal{L}\mathbf{f}$,
 - (d) $\mathcal{M}\mathbf{f}$, $\mathcal{M}^1\mathbf{f}$ and $\mathcal{T}\mathbf{f}$.
 4. \mathbf{f} is recovered either from the combination of $\mathcal{L}\mathbf{f}$, $\mathcal{L}^1\mathbf{f}$, $\mathcal{M}\mathbf{f}$ or $\mathcal{T}\mathbf{f}$, $\mathcal{T}^1\mathbf{f}$, $\mathcal{M}\mathbf{f}$.
 5. \mathbf{f} is recovered from $\mathcal{S}\mathbf{f}$.

Our choice of the special tensor fields listed above is not arbitrary. Their forms are motivated by the decomposition $\mathbf{f} = (\text{d}^\perp)^2\varphi + (\text{dd}^\perp)\chi + \text{d}^2\psi$ of a symmetric 2-tensor field \mathbf{f} discussed in [15, Theorem 4.2]. In the straight-line setup considered in [15], the scalar functions φ , χ , and ψ are recovered explicitly from the knowledge of the longitudinal, mixed, and transverse ray transforms of \mathbf{f} , respectively. The situation is different in the V-line setting, as discussed in Theorem 1 below. Namely, the function φ (when $\mathbf{f} = \text{d}^2\varphi$) can be recovered explicitly from the longitudinal or mixed V-line transform of \mathbf{f} , and similar results hold for the other types of special tensor fields.

On the other hand, the special tensor fields $\mathbf{f} = \text{d}\mathbf{g}$ and $\mathbf{f} = \text{d}^\perp\mathbf{g}$ correspond to the decomposition $\mathbf{f} = \text{d}^\perp\tilde{\mathbf{g}} + \text{d}\mathbf{g}$, which can be obtained by adjusting the terms of the decomposition from [15, Theorem 4.2] mentioned above. It is known that $\text{d}\mathbf{g}$ is in the kernel of the longitudinal (straight line) ray transform. However, $\text{d}\mathbf{g}$ is NOT in the kernel of the longitudinal V-line transform. Moreover, as we have shown in [8], any potential tensor fields $\mathbf{f} = \text{d}\mathbf{g}$ can be recovered from the combination of the longitudinal and mixed VLTs. Similarly, $\text{d}^\perp\mathbf{g}$ is in the kernel of the transverse (straight line) ray transform, but not in the kernel of the transverse V-line transform. Instead, one can recover $\mathbf{f} = \text{d}^\perp\mathbf{g}$ from the combination of the transverse and mixed VLTs of \mathbf{f} .

4.1 Numerical implementation for special kinds of tensor fields

4.1.1 Tensor fields of the form $\mathbf{f} = \text{d}^2\varphi$, $\mathbf{f} = \text{dd}^\perp\varphi$, or $\mathbf{f} = (\text{d}^\perp)^2\varphi$

In this subsection, we consider symmetric 2-tensor fields of the form $\mathbf{f} = \text{d}^2\varphi$, $(\text{d}^\perp)^2\varphi$, or $\text{dd}^\perp\varphi$, where φ is a scalar function. We reconstruct φ from specific VLTs, depending on the form of \mathbf{f} . Our reconstructions of φ when $\mathbf{f} = \text{d}^2\varphi$ and when $\mathbf{f} = (\text{d}^\perp)^2\varphi$ are almost identical. Therefore, to save space and avoid repetition, we present below only the numerical results corresponding to the first case. We also demonstrate the numerical reconstruction of φ when $\mathbf{f} = \text{dd}^\perp\varphi$. To avert redundancy, we have not included reconstructions without noise in this case.

Theorem 1. *Let φ be a twice differentiable, compactly supported function, that is, $\varphi \in C_c^2(D_1)$.*

- (a) *If \mathbf{f} is a symmetric 2-tensor field of the form $\mathbf{f} = \text{d}^2\varphi$, then it can be reconstructed explicitly in terms of $\mathcal{L}\mathbf{f}$ or $\mathcal{M}\mathbf{f}$, using the following formulas:*

$$\varphi(\mathbf{x}) = \frac{1}{2u_2} \int_0^\infty \mathcal{L}\mathbf{f}(\mathbf{x} + s\mathbf{e}_2) ds = -\frac{1}{2u_2} \int_0^\infty \mathcal{M}\mathbf{f}(\mathbf{x} + s\mathbf{e}_1) ds. \quad (28)$$

(b) If \mathbf{f} is a symmetric 2-tensor field of the form $\mathbf{f} = (\mathbf{d}^\perp)^2 \varphi$, then it can be reconstructed explicitly in terms of $\mathcal{T}\mathbf{f}$ or $\mathcal{M}\mathbf{f}$, using the following formulas:

$$\varphi(\mathbf{x}) = \frac{1}{2u_2} \int_0^\infty \mathcal{T}\mathbf{f}(\mathbf{x} + s\mathbf{e}_2) ds = \frac{1}{2u_2} \int_0^\infty \mathcal{M}\mathbf{f}(\mathbf{x} + s\mathbf{e}_1) ds. \quad (29)$$

(c) If \mathbf{f} is a symmetric 2-tensor field of the form $\mathbf{f} = \mathbf{d}\mathbf{d}^\perp \varphi$, then it can be reconstructed explicitly in terms of $\mathcal{L}\mathbf{f}$ or $\mathcal{T}\mathbf{f}$, using the following formulas:

$$\varphi(\mathbf{x}) = \frac{1}{2u_2} \int_0^\infty \mathcal{L}\mathbf{f}(\mathbf{x} + s\mathbf{e}_1) ds = -\frac{1}{2u_2} \int_0^\infty \mathcal{T}\mathbf{f}(\mathbf{x} + s\mathbf{e}_1) ds. \quad (30)$$

In this case, \mathbf{f} can also be reconstructed from $\mathcal{M}\mathbf{f}$ by solving the following second order partial differential equation for φ (with appropriate initial/boundary conditions):

$$(1 + 2u_1^2) \frac{\partial^2 \varphi}{\partial x_1^2} + (u_1^2 - u_2^2) \frac{\partial^2 \varphi}{\partial x_2^2} = -\frac{1}{u_2} \mathcal{X}_{\mathbf{e}_2} (D_u D_v \mathcal{M}\mathbf{f})(\mathbf{x}). \quad (31)$$

Let $\mathbf{f} = \mathbf{d}^2 \varphi$. Figure 2 shows the results of the numerical implementation of formula (28) for a non-smooth phantom, with V-lines corresponding to $\mathbf{u} = (\cos \pi/4, \sin \pi/4)$.

Here and in all other numerical implementations presented in the paper, we test the effectiveness of the inversion algorithm by adding to the data different amounts of Gaussian noise. Figure 2 includes reconstructions with 20% of additive Gaussian noise. Also, here and in all upcoming sections, we include a table describing the relative error of the reconstructions, calculated as follows:

$$\text{Relative error of } \varphi = \frac{\|\varphi_{\text{original}} - \varphi_{\text{rec}}\|_2}{\|\varphi_{\text{original}}\|_2} \times 100\%,$$

where $\|\varphi\|_2$ denotes the spectral norm, i.e. the maximum singular value of the matrix φ .

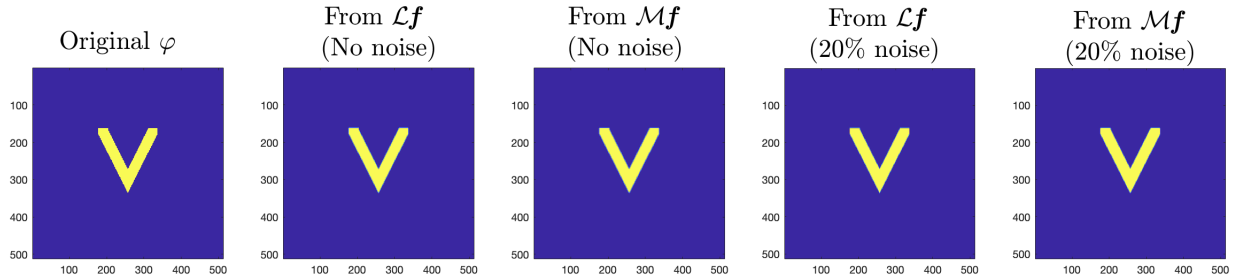


Figure 2: Recovery of φ when $\mathbf{f} = \mathbf{d}^2 \varphi$, using formula (28).

From $\mathcal{L}\mathbf{f}$ (No noise)	From $\mathcal{M}\mathbf{f}$ (No noise)	From $\mathcal{L}\mathbf{f}$ (20% noise)	From $\mathcal{M}\mathbf{f}$ (20% noise)
5.60%	4.99%	10.91%	36.61%

Table 3: Relative errors of reconstruction of φ from $\mathcal{L}\mathbf{f}$ or $\mathcal{M}\mathbf{f}$ when $\mathbf{f} = \mathbf{d}^2 \varphi$.

Since visually all reconstructions in Figure 2 look the same, we include below the images of the differences of the original image and the reconstructions, explaining the relative errors in Table 3. We skip this part for the other reconstructions in this paper.

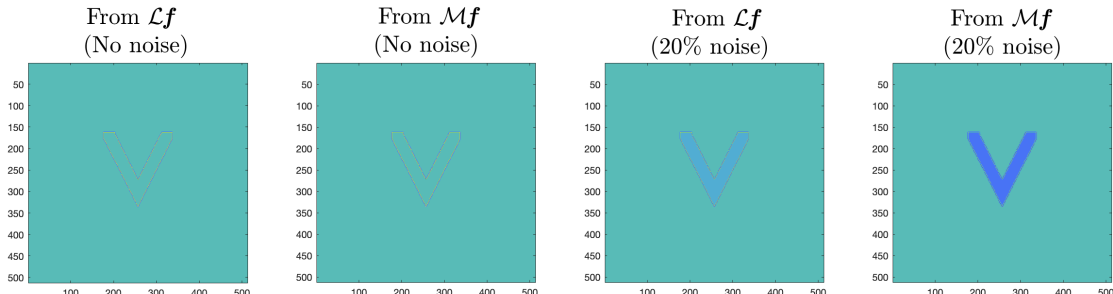


Figure 3: Graphical representation of $\varphi_{\text{original}} - \varphi_{\text{rec}}$. The colormap is scaled according to the minimum and maximum values of all four pictures.

Let $\mathbf{f} = \text{dd}^\perp \varphi$. The reconstructions using formulas (30) and (31) are shown in Figures 4, 5, 6. Depending on the choice of \mathbf{u} , the PDE appearing in (31) is elliptic ($\mathbf{u} = (\cos \pi/6, \sin \pi/6)$), parabolic ($\mathbf{u} = (\cos \pi/4, \sin \pi/4)$), or hyperbolic ($\mathbf{u} = (\cos \pi/3, \sin \pi/3)$). The numerical solutions of such PDEs are discussed in Section 3. Since the reconstructions are quite good even with 10% of added noise, we have not included the images of reconstructions using data without noise. The relative errors of reconstructions without noise are included in the appropriate tables.

Remark 6. *To recover φ from $\mathcal{M}\mathbf{f}$ when $\mathbf{f} = \text{dd}^\perp \varphi$, we need to solve the PDE (31), where the source term $D_{\mathbf{u}}D_{\mathbf{v}}\mathcal{M}\mathbf{f}$ is known to us. In particular, it is known (see [8]) that the source term is supported inside a disc contained in the square domain of the data. We use this fact to assign the value of 0 to all entries of $D_{\mathbf{u}}D_{\mathbf{v}}\mathcal{M}\mathbf{f}$ within 5 pixels from the boundary of that domain. This helps to substantially reduce the artifacts in the reconstruction due to the errors of numerical differentiation at the boundary of the domain.*

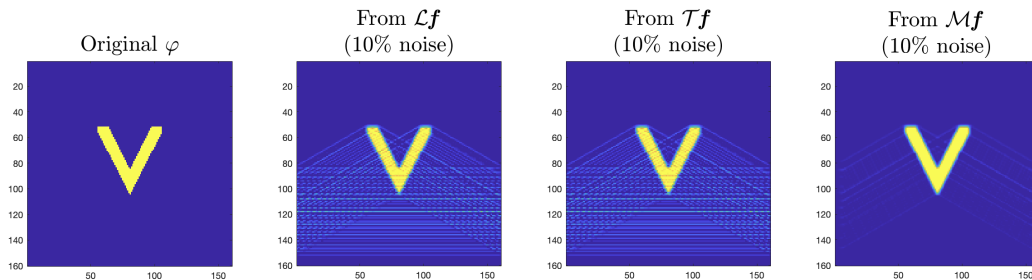


Figure 4: Recovery of φ when $\mathbf{f} = \text{dd}^\perp \varphi$, $u_1 > u_2$ (elliptic), with 10% noise, using (30), (31).

The horizontal artifacts in the reconstructions in Figure 4 are due to the cut of the transform data at the boundary (and its absence outside of) the square $[-1, 1] \times [-1, 1]$. In fact, the essential part here is the cut of the data along the right side of the square (see formula 30). Such artifacts can be easily eliminated by adjusting the size of the data domain according to the support of the

image field, so that the part of the boundary, where the data is cut, is located below the support of the image field.

	From $\mathcal{L}f$	From $\mathcal{T}f$	From $\mathcal{M}f$
No Noise	79.09%	79.09%	12.37%
10% Noise	81.40%	80.66%	17.45%

Table 4: Relative errors of reconstruction of φ from $\mathcal{L}f$, $\mathcal{T}f$ or $\mathcal{M}f$ when $f = dd^\perp\varphi$ and $u_1 > u_2$.

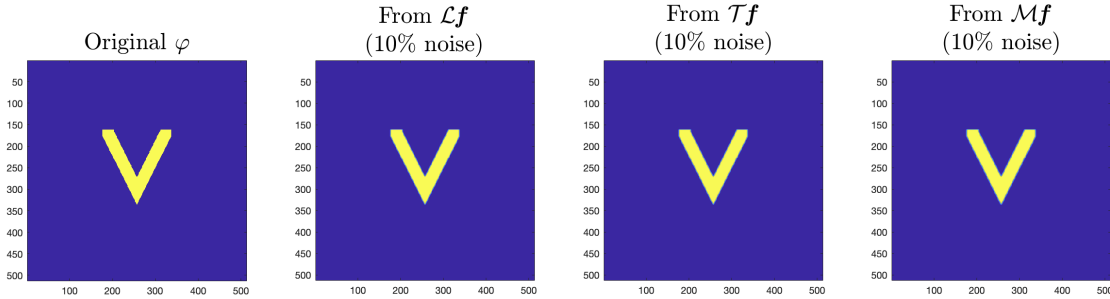


Figure 5: Recovery of φ when $f = dd^\perp\varphi$, $u_1 = u_2$ (parabolic), with 10% noise, using (30), (31).

	From $\mathcal{L}f$	From $\mathcal{T}f$	From $\mathcal{M}f$
No Noise	4.99%	4.99%	6.03%
10% Noise	7.48%	5.13%	7.65%

Table 5: Relative errors of reconstruction of φ from $\mathcal{L}f$, $\mathcal{T}f$ or $\mathcal{M}f$ when $f = dd^\perp\varphi$ and $u_1 = u_2$.

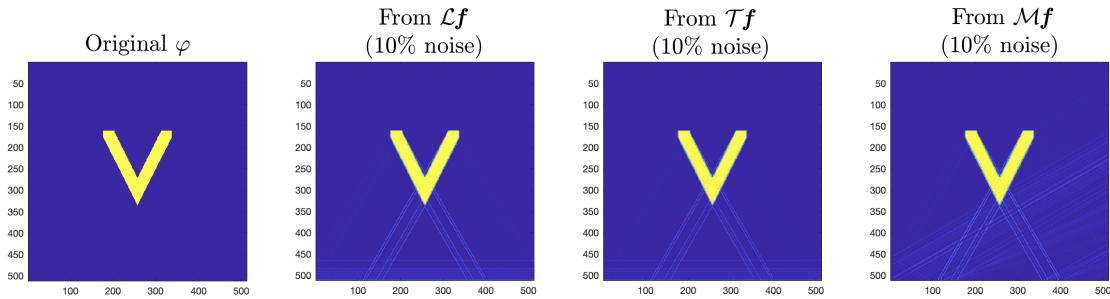


Figure 6: Recovery of φ when $f = dd^\perp\varphi$, $u_1 < u_2$ (hyperbolic), with 10% noise, using (30), (31).

4.1.2 Tensor fields of the form $f = dg$ or $f = d^\perp g$

In this subsection, we consider 2-tensor fields of the form $f = dg$ or $f = d^\perp g$, where g is a vector field. We validate the methods obtained in [8] for efficient reconstructions of g using certain

	From $\mathcal{L}\mathbf{f}$	From $\mathcal{T}\mathbf{f}$	From $\mathcal{M}\mathbf{f}$
No Noise	12.09%	12.09%	7.89%
10% Noise	30.39%	14.02%	14.66%

Table 6: Relative errors of reconstruction of φ from $\mathcal{L}\mathbf{f}$, $\mathcal{T}\mathbf{f}$ or $\mathcal{M}\mathbf{f}$ when $\mathbf{f} = \text{d}\text{d}^\perp\varphi$ and $u_1 < u_2$.

combinations of the VLTs of \mathbf{f} with and without noise. Since the reconstructions in the case $\mathbf{f} = \text{d}^\perp\mathbf{g}$ are almost identical to those in the case $\mathbf{f} = \text{d}\mathbf{g}$, we have not included the reconstruction images for $\text{d}^\perp\mathbf{g}$.

Theorem 2. Let $\mathbf{g} = (g_1, g_2)$ be a vector field with components $g_i(\mathbf{x}) \in C_c^2(D_1)$, for $i = 1, 2$.

- (a) If \mathbf{f} is a symmetric 2-tensor field of the form $\mathbf{f} = \text{d}\mathbf{g}$, then it can be recovered explicitly in terms of $\mathcal{L}\mathbf{f}$ and $\mathcal{M}\mathbf{f}$ as follows:

$$g_2(\mathbf{x}) = -\frac{1}{2u_2}\mathcal{L}\mathbf{f}(\mathbf{x}), \quad (32)$$

and g_1 can be recovered by solving a second-order partial differential equation

$$2u_1^2\frac{\partial^2 g_1}{\partial x_1^2}(\mathbf{x}) + (u_1^2 - u_2^2)\frac{\partial^2 g_1}{\partial x_2^2}(\mathbf{x}) = -\frac{1}{2u_2}D_u D_v h(\mathbf{x}), \quad (33)$$

where $h(\mathbf{x}) = 2\mathcal{M}\mathbf{f}(\mathbf{x}) + \mathcal{V}\left(\frac{\partial g_2}{\partial x_1}\right)(\mathbf{x})$ with additional homogeneous boundary (or initial) conditions. More explicitly, we have the following three cases:

- (i) When $u_1^2 > u_2^2$, we have an elliptic PDE (33) with homogeneous boundary conditions.
(ii) When $u_1^2 = u_2^2$, the partial differential equation (33) becomes:

$$2u_1^2\frac{\partial^2 g_1}{\partial x_1^2}(\mathbf{x}) = -\frac{1}{2u_2}D_u D_v h(\mathbf{x}), \quad (34)$$

which can be solved for g_1 by integrating twice along \mathbf{e}_1 -direction.

- (iii) When $u_1^2 < u_2^2$, we have a hyperbolic PDE (33), which can be solved by choosing appropriate initial conditions on g_1 (for instance, we can take $g_1(a, y) = 0$ and $\frac{\partial g_1}{\partial x_1}(a, y) = 0$, for $y \in \mathbb{R}$ and any fixed $a \in \mathbb{R} \setminus [-1, 1]$).

- (b) If \mathbf{f} is a symmetric 2-tensor field of the form $\mathbf{f} = \text{d}^\perp\mathbf{g}$, then it can be recovered explicitly in terms of $\mathcal{T}\mathbf{f}$ and $\mathcal{M}\mathbf{f}$ as follows:

$$g_1(\mathbf{x}) = \frac{1}{2u_2}\mathcal{T}\mathbf{f}(\mathbf{x}) \quad (35)$$

and g_2 can be recovered by solving the following second-order partial differential equation (equipped with appropriate boundary or initial conditions):

$$2u_1^2\frac{\partial^2 g_2}{\partial x_1^2}(\mathbf{x}) + (u_1^2 - u_2^2)\frac{\partial^2 g_2}{\partial x_2^2}(\mathbf{x}) = -\frac{1}{2u_2}D_u D_v \tilde{h}(\mathbf{x}), \quad (36)$$

where $\tilde{h}(\mathbf{x}) = -2\mathcal{M}\mathbf{f}(\mathbf{x}) - \mathcal{V}\left(\frac{\partial g_1}{\partial x_1}\right)(\mathbf{x})$.

In Figures 7, 8, 9, g_2 is reconstructed directly from $\mathcal{L}f$ (see (32)), while the recovery of g_1 requires either solving an elliptic ($\mathbf{u} = (\cos \pi/6, \sin \pi/6)$) or hyperbolic ($\mathbf{u} = (\cos \pi/3, \sin \pi/3)$) PDE (33), or double integration solving the parabolic PDE (34) (for $\mathbf{u} = (\cos \pi/4, \sin \pi/4)$). Figure 10 presents the reconstructions from data with 20% added noise. The same algorithms are used in Figures 11, 12, 13, 14 for the non-smooth phantom.

Remark 7. To recover g_1 when $\mathbf{f} = d\mathbf{g}$, we are solving PDEs, in which the source term $D_{\mathbf{u}}D_{\mathbf{v}}h$ is known to us. Following the ideas discussed in Remark 6, we assign the value of 0 to all entries of $D_{\mathbf{u}}D_{\mathbf{v}}h$ within 5 pixels from the boundary of the data domain.

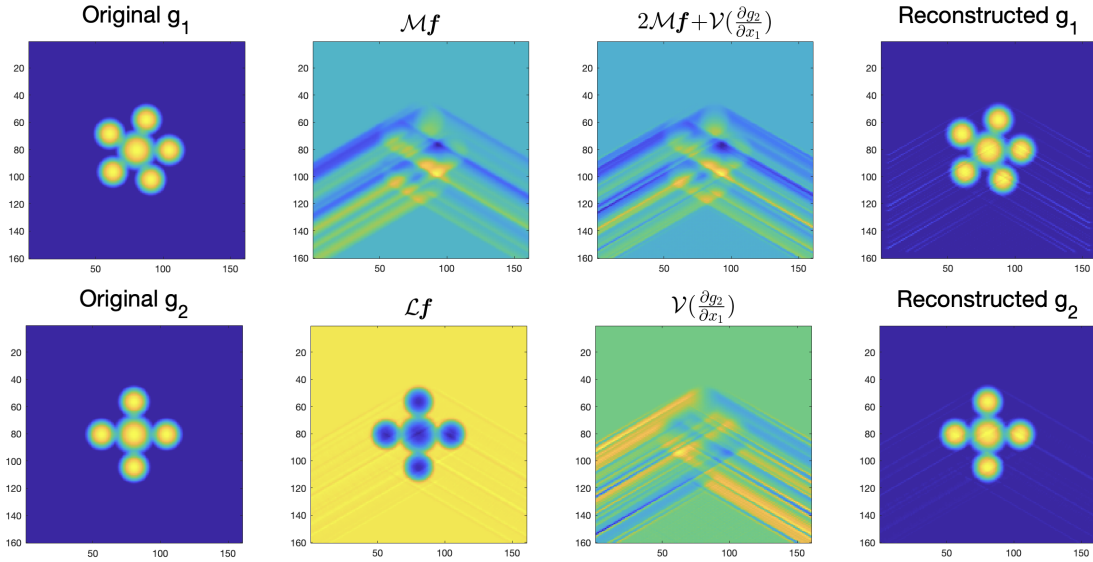


Figure 7: Recovery of \mathbf{g} from $\mathcal{L}f$ and $\mathcal{M}f$ when $\mathbf{f} = d\mathbf{g}$, $u_1 > u_2$ (elliptic), using (32), (33).

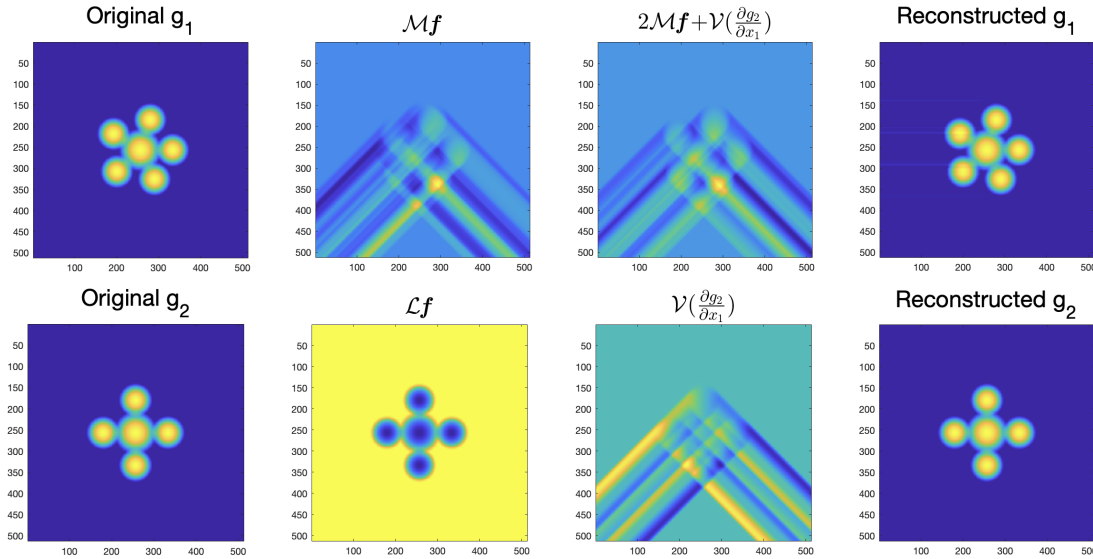


Figure 8: Recovery of \mathbf{g} from $\mathcal{L}f$ and $\mathcal{M}f$ when $\mathbf{f} = d\mathbf{g}$, $u_1 = u_2$ (parabolic), using (32), (34).

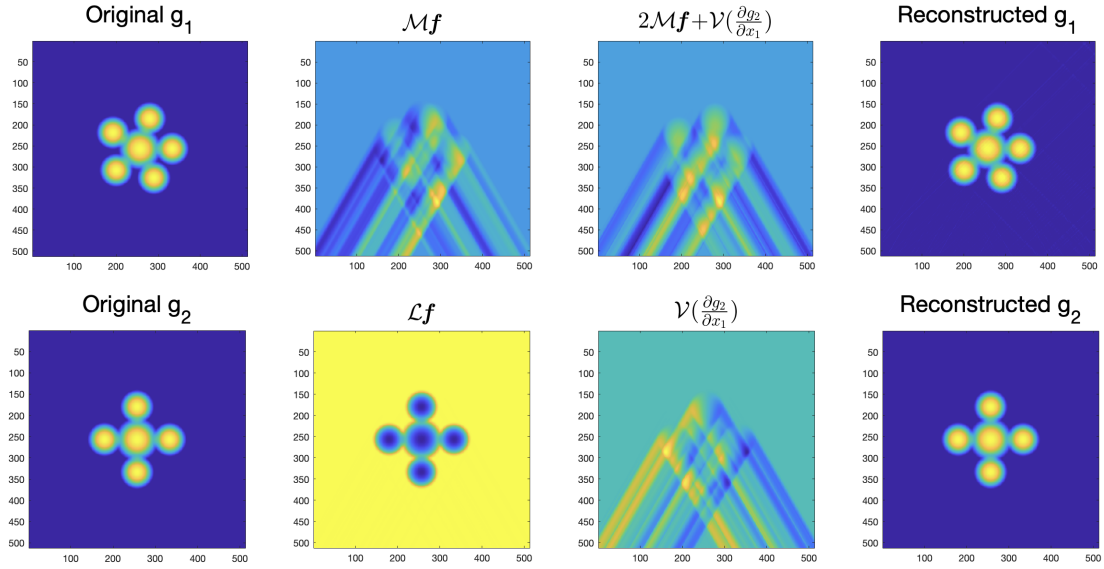


Figure 9: Recovery of g from $\mathcal{L}f$ and $\mathcal{M}f$ when $f = dg$, $u_1 < u_2$ (hyperbolic), using (32), (33).

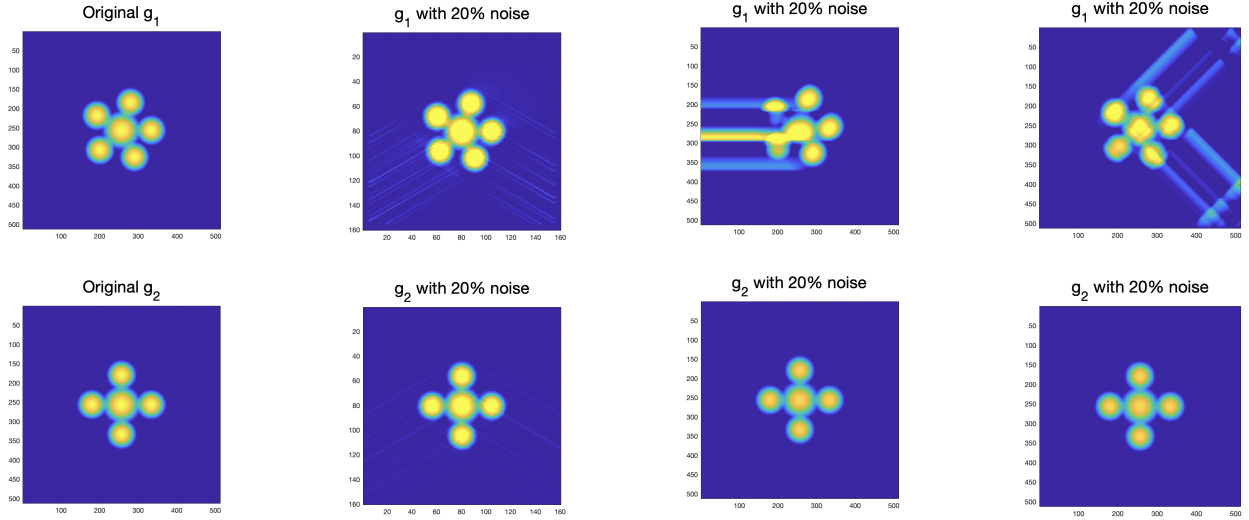


Figure 10: Column 1: original g_1, g_2 ; Column 2: reconstr. g_1, g_2 , $u_1 > u_2$ (elliptic), 20% noise; Column 3: reconstr. g_1, g_2 , $u_1 = u_2$ (parabolic), 20% noise; Column 4: reconstr. g_1, g_2 , $u_1 < u_2$ (hyperbolic), 20% noise.

g	20% Noise - Elliptic	20% Noise - Parabolic	20% Noise - Hyperbolic
g_1	33.75%	107.46%	37.59%
g_2	13.80%	8.72%	8.72%

Table 7: Relative errors of reconstruction of g from $\mathcal{L}f$ and $\mathcal{M}f$ when $f = dg$.

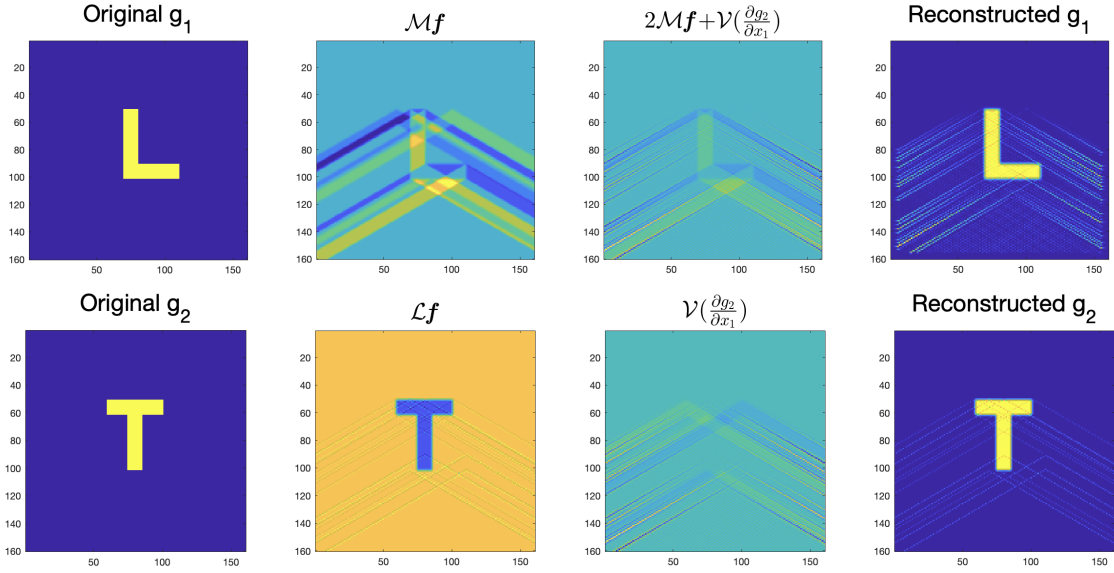


Figure 11: Recovery of g from $\mathcal{L}f$ and $\mathcal{M}f$ when $f = dg$, $u_1 > u_2$ (elliptic), using (32), (33).

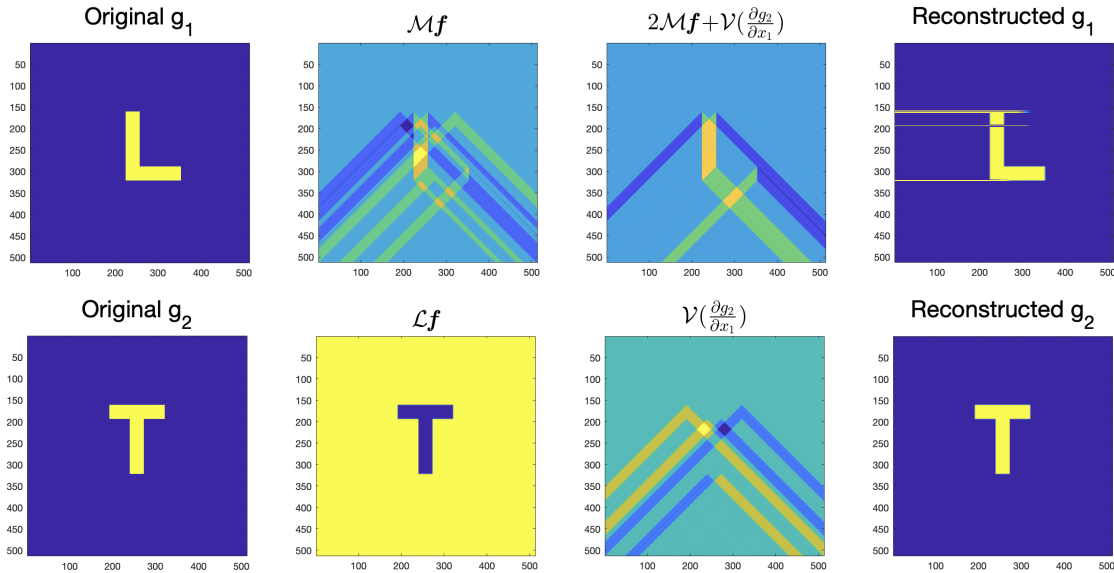


Figure 12: Recovery of g from $\mathcal{L}f$ and $\mathcal{M}f$ when $f = dg$, $u_1 = u_2$ (parabolic), using (32), (34).

The horizontal artifacts in the reconstruction of g_1 in Figure 12 are due to the errors of numerical differentiation of $h(\boldsymbol{x})$ in the right-hand side of equation (34), propagated by the double integration with respect to x_1 . Although visually the horizontal artifacts do not seem to cause a severe distortion of the original image, their strength (i.e. the numerical value of the reconstructed function at the artifact pixels) is quite large, adversely affecting the relative error of the reconstruction (see Table 8).

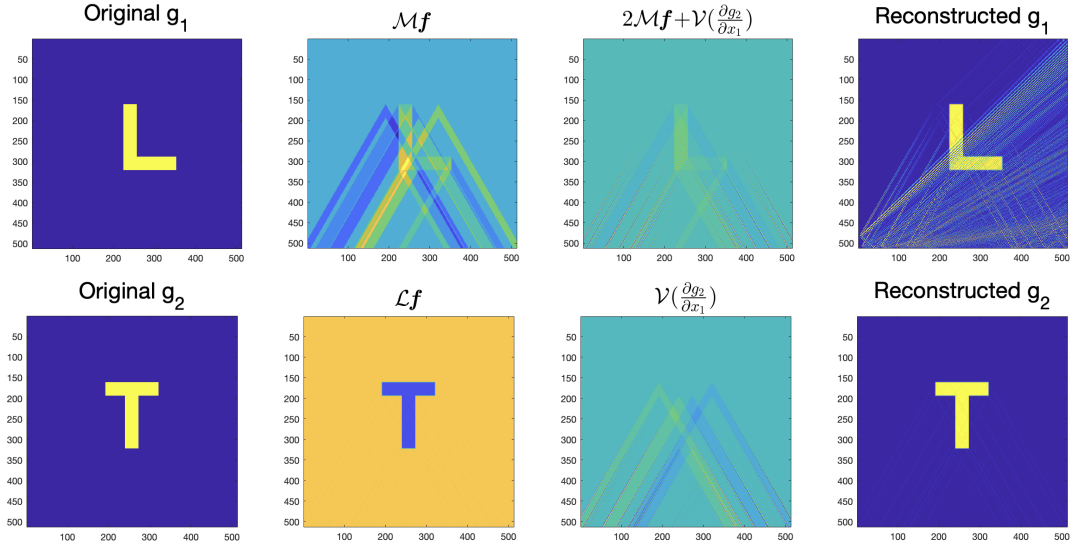


Figure 13: Recovery of g from $\mathcal{L}f$ and $\mathcal{M}f$ when $f = dg$, $u_1 < u_2$ (hyperbolic), using (32),(33).

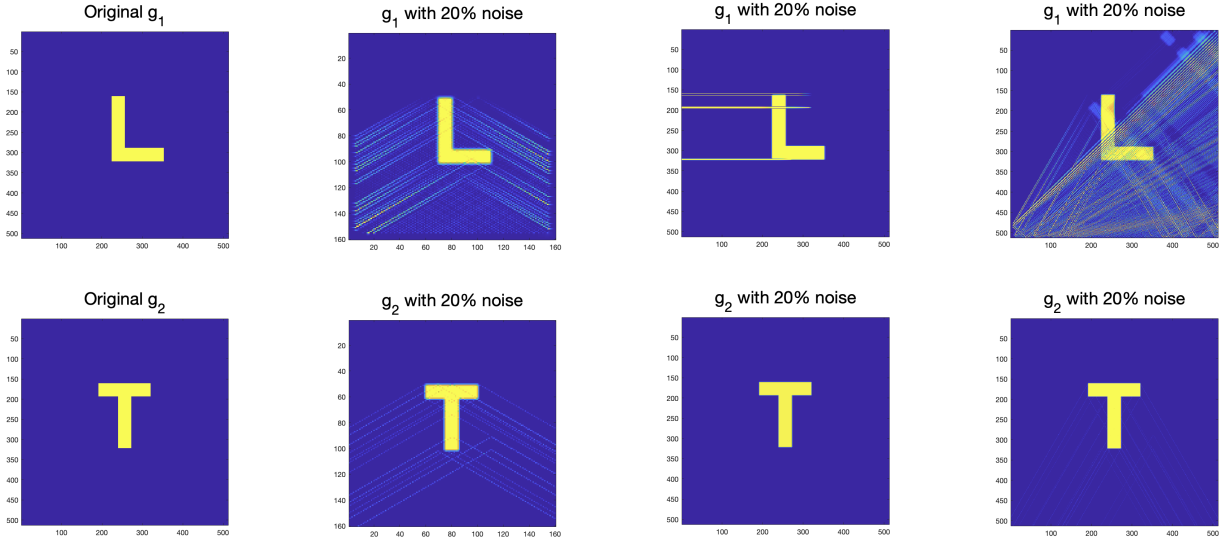


Figure 14: Column 1: original g_1, g_2 ; Column 2: reconstr. g_1, g_2 , $u_1 > u_2$ (elliptic), 20% noise; Column 3: reconstr. g_1, g_2 , $u_1 = u_2$ (parabolic), 20% noise; Column 4: reconstr. g_1, g_2 , $u_1 < u_2$ (hyperbolic), 20% noise.

g	20% Noise - Elliptic	20% Noise - Parabolic	20% Noise -Hyperbolic
g_1	30.54%	820.16%	50.93%
g_2	13.55%	7.80%	15.73%

Table 8: Relative errors of reconstruction of g from $\mathcal{L}f$ and $\mathcal{M}f$ when $f = dg$.

4.2 Full Recovery of \mathbf{f} from $\mathcal{L}\mathbf{f}$, $\mathcal{T}\mathbf{f}$ and $\mathcal{M}\mathbf{f}$

In this subsection, we use $\mathcal{L}\mathbf{f}$, $\mathcal{T}\mathbf{f}$, and $\mathcal{M}\mathbf{f}$ to recover \mathbf{f} . As in the previous sections, we start by discussing the theoretical results for this setup in Theorem 3.

Theorem 3. Consider a symmetric 2-tensor field $\mathbf{f} \in C_c^2(S^2; D_1)$, $\mathbf{e}_1 = (1, 0)$ and $\mathbf{e}_2 = (0, 1)$.

- For $u_1 = u_2$, \mathbf{f} can be recovered from $\mathcal{L}\mathbf{f}$, $\mathcal{T}\mathbf{f}$, and $\mathcal{M}\mathbf{f}$ by

$$f_{11}(\mathbf{x}) = \frac{1}{4u_2} D_u D_v \mathcal{X}_{\mathbf{e}_2} (\mathcal{L}\mathbf{f} + \mathcal{T}\mathbf{f})(\mathbf{x}) - \frac{1}{2u_1} D_u D_v \mathcal{X}_{-\mathbf{e}_1} \mathcal{M}\mathbf{f}(\mathbf{x}), \quad (37)$$

$$f_{12}(\mathbf{x}) = \frac{1}{4u_1} D_u D_v \mathcal{X}_{-\mathbf{e}_1} (\mathcal{L}\mathbf{f} - \mathcal{T}\mathbf{f})(\mathbf{x}), \quad (38)$$

$$f_{22}(\mathbf{x}) = \frac{1}{4u_2} D_u D_v \mathcal{X}_{\mathbf{e}_2} (\mathcal{L}\mathbf{f} + \mathcal{T}\mathbf{f})(\mathbf{x}) + \frac{1}{2u_1} D_u D_v \mathcal{X}_{-\mathbf{e}_1} \mathcal{M}\mathbf{f}(\mathbf{x}). \quad (39)$$

- For $u_1 \neq u_2$, \mathbf{f} can be reconstructed from $\mathcal{L}\mathbf{f}$, $\mathcal{T}\mathbf{f}$, and $\mathcal{M}\mathbf{f}$ as follows.
 f_{12} can be found by solving the elliptic boundary value problem:

$$\begin{cases} a\partial_{x_1}^2 f_{12} + b\partial_{x_2}^2 f_{12} = -g & \text{in } D_1, \\ f_{12} = 0 & \text{on } \partial D_1, \end{cases} \quad (40)$$

where $a = 2u_1^2 [1 + (u_1^2 - u_2^2)] > 0$, $b = (u_1^2 - u_2^2)^2 > 0$, and

$$g = \frac{1}{2u_2} [u_1^2 \partial_{x_1} D_u D_v (\mathcal{T}\mathbf{f} - \mathcal{L}\mathbf{f}) + (u_1^2 - u_2^2) \partial_{x_2} D_u D_v \mathcal{M}\mathbf{f}].$$

f_{11} can be recovered from the knowledge of $\mathcal{L}\mathbf{f}$, $\mathcal{T}\mathbf{f}$, and the reconstructed f_{12} by

$$f_{11} = -\mathcal{X}_{\mathbf{e}_2} [(u_2^2 D_u D_v \mathcal{T}\mathbf{f} - u_1^2 D_u D_v \mathcal{L}\mathbf{f} + 4u_1^2 u_2 \partial_{x_1} f_{12}) / (2u_2(u_1^2 - u_2^2))]. \quad (41)$$

f_{22} can be recovered from $\mathcal{L}\mathbf{f}$, $\mathcal{T}\mathbf{f}$, and the reconstructed f_{11} by

$$f_{22}(\mathbf{x}) = \frac{1}{2u_2} D_u D_v \mathcal{X}_{\mathbf{e}_2} (\mathcal{L}\mathbf{f} + \mathcal{T}\mathbf{f})(\mathbf{x}) - f_{11}(\mathbf{x}). \quad (42)$$

Figure 15 depicts the reconstructions of Phantom 2 using formulas (37), (38), (39). Figure 16 shows the corresponding reconstructions in the presence of different levels of noise.

\mathbf{f}	No noise	5% Noise	10% Noise	20% Noise
f_{11}	5.22%	85.56%	194.44%	452.72%
f_{12}	9.42%	30.25%	68.14%	158.89%
f_{22}	8.15%	65.07%	146.95%	344.88%

Table 9: Relative errors of reconstructing f_{11} , f_{12} , f_{22} from $\mathcal{L}\mathbf{f}$, $\mathcal{M}\mathbf{f}$, $\mathcal{T}\mathbf{f}$, $\mathbf{u} = (\cos \pi/4, \sin \pi/4)$.

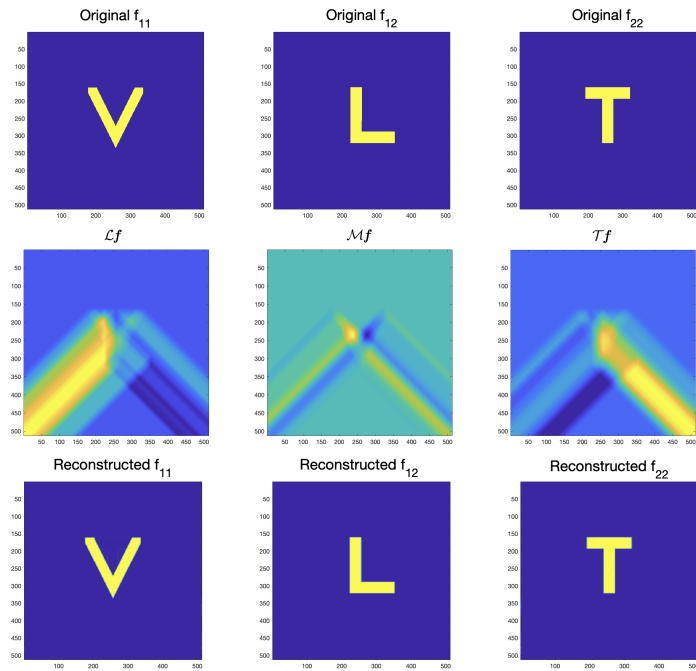


Figure 15: Reconstruction of f from $\mathcal{L}f, \mathcal{M}f, \mathcal{T}f$, $u = (\cos \pi/4, \sin \pi/4)$, using formulas (37), (38), (39).

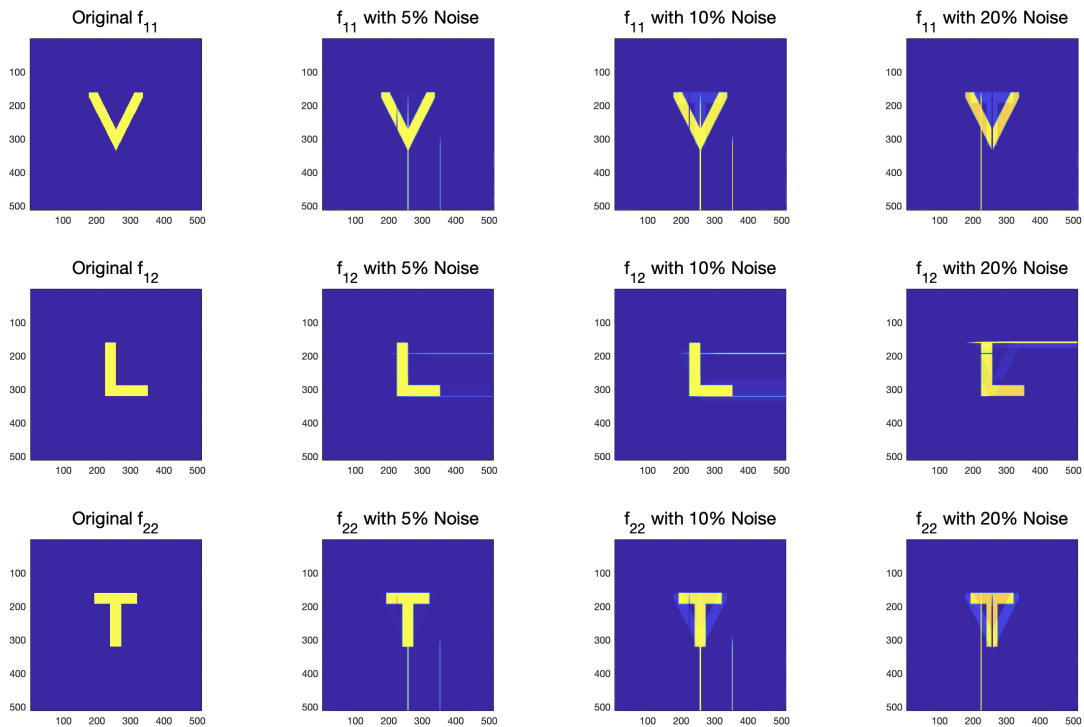


Figure 16: Reconstructions from $\mathcal{L}f, \mathcal{M}f, \mathcal{T}f$, $u = (\cos \pi/4, \sin \pi/4)$ with 5%, 10%, 20% noise.

We took $\mathbf{u} = (\cos \pi/3, \sin \pi/3)$ for implementations of (40), (41), and (42) shown in Figures 17 and 19 for the smooth and non-smooth phantoms, respectively. Corresponding reconstructions in the presence of various levels of noise are presented in Figures 18 and 20.

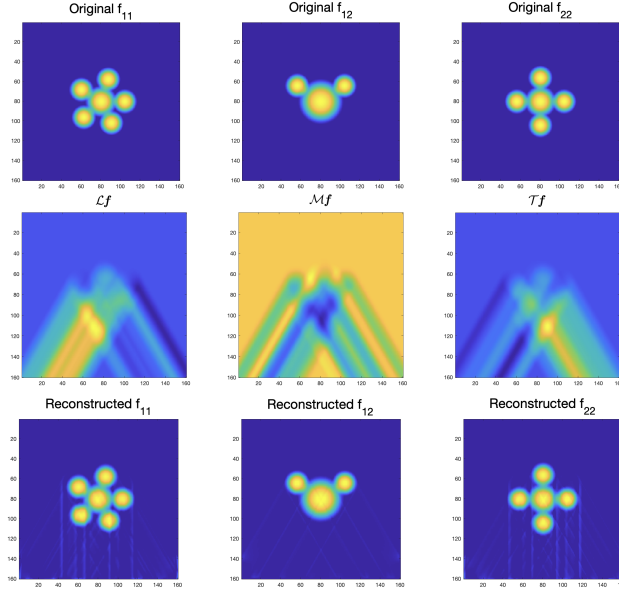


Figure 17: Reconstructions of \mathbf{f} from $\mathcal{L}\mathbf{f}$, $\mathcal{M}\mathbf{f}$, $\mathcal{T}\mathbf{f}$, $\mathbf{u} = (\cos \pi/3, \sin \pi/3)$, using formulas (40), (41), (42).

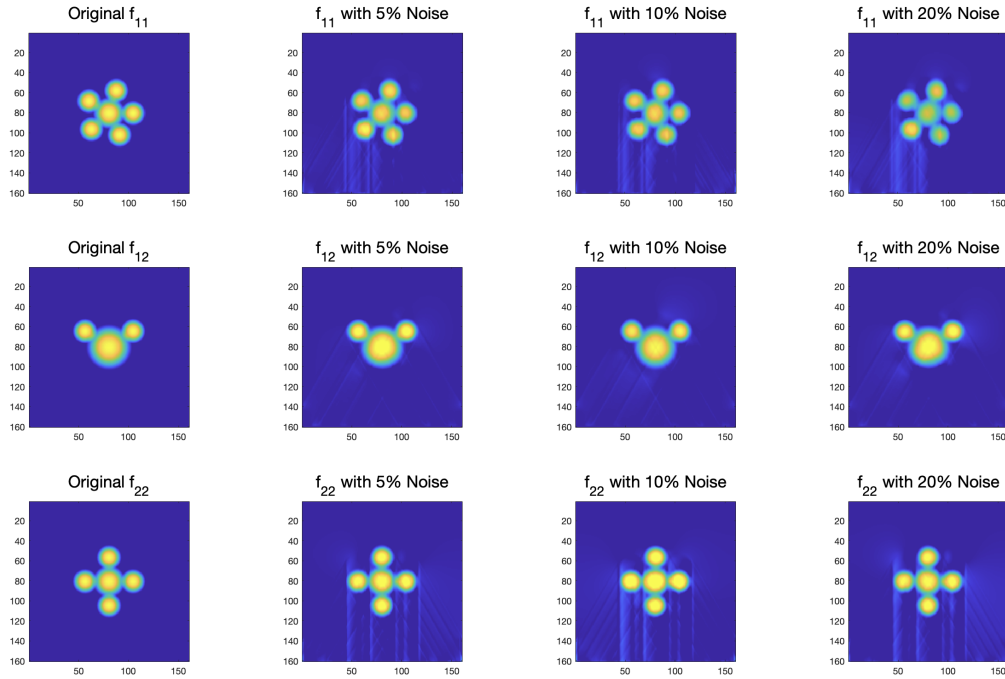


Figure 18: Reconstructions from $\mathcal{L}\mathbf{f}$, $\mathcal{M}\mathbf{f}$, $\mathcal{T}\mathbf{f}$, $\mathbf{u} = (\cos \pi/3, \sin \pi/3)$, 5%, 10% and 20% noise.

\mathbf{f}	No noise	5% Noise	10% Noise	20% Noise
f_{11}	8.49%	16.27%	18.60%	30.64%
f_{12}	1.84%	8.62%	6.45%	9.54%
f_{22}	8.77%	15.20%	25.15%	21.34%

Table 10: Relative errors of reconstructing the components of the smooth Phantom 1 using $\mathcal{L}\mathbf{f}$, $\mathcal{M}\mathbf{f}$, $\mathcal{T}\mathbf{f}$, and $\mathbf{u} = (\cos \pi/3, \sin \pi/3)$.

\mathbf{f}	No noise	5% Noise	10% Noise	20% Noise
f_{11}	321.77%	293.14%	338.85%	450.29%
f_{12}	16.26%	16.29%	18.79%	24.92%
f_{22}	234.58%	262.40%	273.35%	257.46%

Table 11: Relative errors of reconstructing the components of the non-smooth Phantom 2, using $\mathcal{L}\mathbf{f}$, $\mathcal{M}\mathbf{f}$, $\mathcal{T}\mathbf{f}$, and $\mathbf{u} = (\cos \pi/3, \sin \pi/3)$.

In our inversion formulas stated in Theorem 3, many terms include successive applications of differentiation and integration operators. It is easy to check that these operators commute, and one can choose the order in which they are applied to the data. In all results presented in this paper, the computations of terms like that are performed by applying the differentiation(s) first, followed by the integration. We have also numerically implemented some of these inversion formulas using the opposite order of the operators. However, the reconstructions using the latter approach were not much different, so we have not included them in the article.

The alternatives discussed above are common in numerical inversions of Radon type transforms. Similar situations appear, for example, in the selection between filtered and ρ -filtered backprojection formulas for inversion of the (classical) Radon transform (e.g. see [23]) and the spherical Radon transform (e.g. see [10]). The systematic analysis and comparison of the two approaches are beyond the scope of this work and are subject of future research.

The artifacts appearing in the reconstructions in Figures 16, 19, 20 can be explained just like those in the reconstruction of g_1 in Figure 12. Namely, they are caused by the errors of numerical differentiation, propagated by integration with respect to x_1 (horizontal artifacts), or with respect to x_2 (vertical artifacts). Although visually they do not seem to alter the original image too much, their strengths are quite large, substantially increasing the relative errors of the reconstructions (see Tables 9, 11). It is also worth pointing out, that the reconstructions of the smooth phantoms using the same algorithms have much milder artifacts and much smaller relative errors.

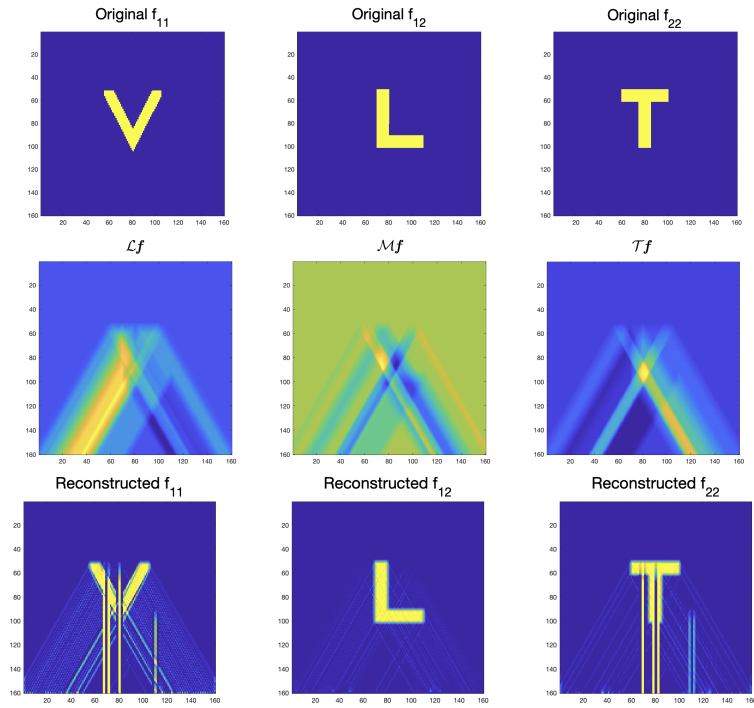


Figure 19: Reconstructions of f from $\mathcal{L}f$, $\mathcal{M}f$, $\mathcal{T}f$, $\mathbf{u} = (\cos \pi/3, \sin \pi/3)$, using formulas (40), (41), (42).

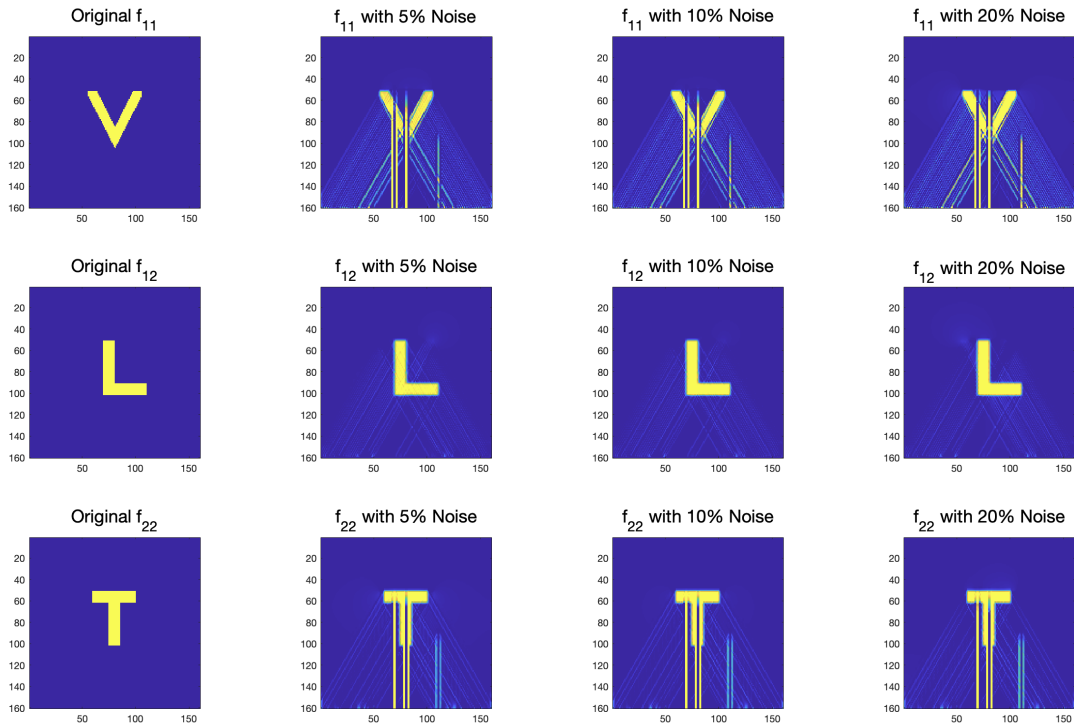


Figure 20: Reconstructions from $\mathcal{L}f$, $\mathcal{M}f$, $\mathcal{T}f$, $\mathbf{u} = (\cos \pi/3, \sin \pi/3)$, 5%, 10% and 20% noise.

4.3 Recovery of tensor fields from first moment VLTs

This subsection is devoted to the full recovery of \mathbf{f} from various combinations of its V-line transforms and their first moments. The reconstruction of the unknown tensor field can be obtained from different subsets of transforms involving first moments, such as $\{\mathcal{L}\mathbf{f}, \mathcal{L}^1\mathbf{f}, \mathcal{T}\mathbf{f}\}$, $\{\mathcal{T}\mathbf{f}, \mathcal{T}^1\mathbf{f}, \mathcal{L}\mathbf{f}\}$, $\{\mathcal{M}\mathbf{f}, \mathcal{M}^1\mathbf{f}, \mathcal{L}\mathbf{f}\}$, $\{\mathcal{M}\mathbf{f}, \mathcal{M}^1\mathbf{f}, \mathcal{T}\mathbf{f}\}$, $\{\mathcal{L}\mathbf{f}, \mathcal{L}^1\mathbf{f}, \mathcal{M}\mathbf{f}\}$, or $\{\mathcal{T}\mathbf{f}, \mathcal{T}^1\mathbf{f}, \mathcal{M}\mathbf{f}\}$. Here, we discuss only two subsets $\{\mathcal{L}\mathbf{f}, \mathcal{L}^1\mathbf{f}, \mathcal{T}\mathbf{f}\}$ and $\{\mathcal{L}\mathbf{f}, \mathcal{L}^1\mathbf{f}, \mathcal{M}\mathbf{f}\}$, as the other combinations yield results similar to one of these cases. More specifically, we discuss the recovery of \mathbf{f} from $\{\mathcal{L}\mathbf{f}, \mathcal{L}^1\mathbf{f}, \mathcal{T}\mathbf{f}\}$ when $\mathbf{u} = (\cos \pi/3, \sin \pi/3)$, and from $\{\mathcal{L}\mathbf{f}, \mathcal{L}^1\mathbf{f}, \mathcal{M}\mathbf{f}\}$ when $\mathbf{u} = (\cos \pi/4, \sin \pi/4)$.

Theorem 4. *If $u_1 \neq u_2$, then $\mathbf{f} \in C_c^2(S^2; D_1)$ can be recovered from $\mathcal{L}\mathbf{f}$, $\mathcal{L}^1\mathbf{f}$, and $\mathcal{T}\mathbf{f}$ by*

$$f_{12}(\mathbf{x}) = \frac{1}{4u_1^2} \partial_{x_2} \mathcal{X}_{e_1} \left[D_u D_v \mathcal{L}^1 \mathbf{f} + \left(D_u + D_v + \frac{1}{u_2} D_u D_v \mathcal{X}_{e_2} \right) \mathcal{L} \mathbf{f} \right] (\mathbf{x}), \quad (43)$$

$$f_{11}(\mathbf{x}) = \frac{1}{2(u_2^2 - u_1^2)} \left[D_u D_v \mathcal{L}^1 \mathbf{f} + (D_u + D_v) \mathcal{L} \mathbf{f} + u_2 D_u D_v \mathcal{X}_{e_2} (\mathcal{L} \mathbf{f} + \mathcal{T} \mathbf{f}) \right] (\mathbf{x}), \quad (44)$$

$$f_{22}(\mathbf{x}) = \frac{1}{2(u_1^2 - u_2^2)} \left[D_u D_v \mathcal{L}^1 \mathbf{f} + (D_u + D_v) \mathcal{L} \mathbf{f} + \frac{u_1^2}{u_2} D_u D_v \mathcal{X}_{e_2} (\mathcal{L} \mathbf{f} + \mathcal{T} \mathbf{f}) \right] (\mathbf{x}). \quad (45)$$

Theorem 5. *The tensor field $\mathbf{f} \in C_c^2(S^2; D_1)$ can be recovered from $\mathcal{L}\mathbf{f}$, $\mathcal{L}^1\mathbf{f}$, and $\mathcal{M}\mathbf{f}$ by*

$$f_{12}(\mathbf{x}) = \frac{1}{4u_1^2} \partial_{x_2} \mathcal{X}_{e_1} \left[D_u D_v \mathcal{L}^1 \mathbf{f} + \left(D_u + D_v + \frac{1}{u_2} D_u D_v \mathcal{X}_{e_2} \right) \mathcal{L} \mathbf{f} \right] (\mathbf{x}), \quad (46)$$

$$f_{11}(\mathbf{x}) = -\frac{1}{2} \left\{ D_u D_v \mathcal{L}^1 \mathbf{f} + (D_u + D_v) \mathcal{L} \mathbf{f} - \frac{u_2}{u_1^2} D_u D_v \mathcal{X}_{-e_1} [(u_1^2 - u_2^2) \mathcal{V}(f_{12}) - \mathcal{M} \mathbf{f}] \right\} (\mathbf{x}), \quad (47)$$

$$f_{22}(\mathbf{x}) = -\frac{1}{2} \left\{ D_u D_v \mathcal{L}^1 \mathbf{f} + (D_u + D_v) \mathcal{L} \mathbf{f} + \frac{1}{u_2} D_u D_v \mathcal{X}_{-e_1} [(u_1^2 - u_2^2) \mathcal{V}(f_{12}) - \mathcal{M} \mathbf{f}] \right\} (\mathbf{x}). \quad (48)$$

Remark 8. *As we have already mentioned in Remark 6, the compactness of the support of \mathbf{f} has certain implications about the support of the VLTs of \mathbf{f} and their derivatives. In particular, it is easy to check that outside of a disc contained in the square domain of reconstruction, the terms $D_u D_v \mathcal{L}^1 \mathbf{f} + (D_u + D_v) \mathcal{L} \mathbf{f}$ and $D_u D_v \mathcal{X}_{e_2} \mathcal{L} \mathbf{f}$ are zero. The same is true for the expressions containing the transverse and mixed transforms in place of the longitudinal VLTs. In our numerical implementations, we assign the value of 0 to all entries of those quantities within 5 pixels from the boundary of the data domain. This reduces the artifacts in the reconstruction due to the errors of numerical differentiation at the boundary of the domain.*

In the case of inversion algorithms applicable to VLTs with different opening angles, the quality of reconstruction often varies based on the opening angle (e.g. see [7]). In particular, the artifacts decrease when the opening angle gets closer to $\pi/2$, which corresponds to the case $\mathbf{u} = (\cos \pi/4, \sin \pi/4)$. This fact is one of the primary reasons of the discrepancy in the quality of reconstructions between Figures 21-24 and Figures 25-28.

Figures 21 and 23 are generated by implementing formulas (44), (43), (45), respectively, for Phantom 1 and 2. Figures 22 and 24 show the effect of noise on the reconstructions.

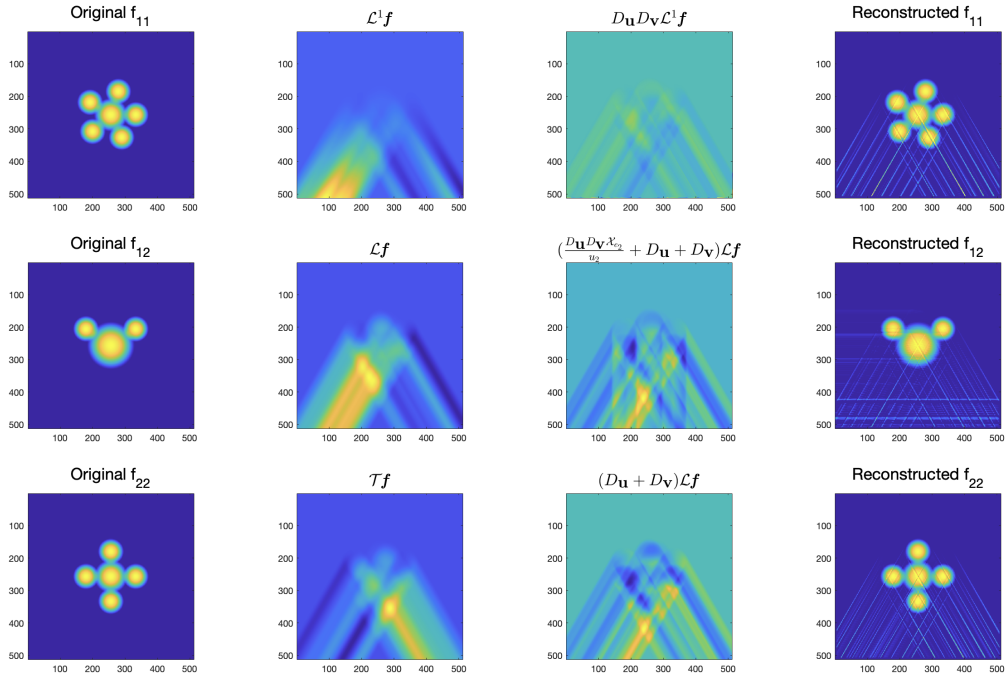


Figure 21: Reconstruction of f from $\mathcal{L}f, \mathcal{L}^1 f, \mathcal{T}f$, $\mathbf{u} = (\cos \pi/3, \sin \pi/3)$ using formulas (44), (43), (45).

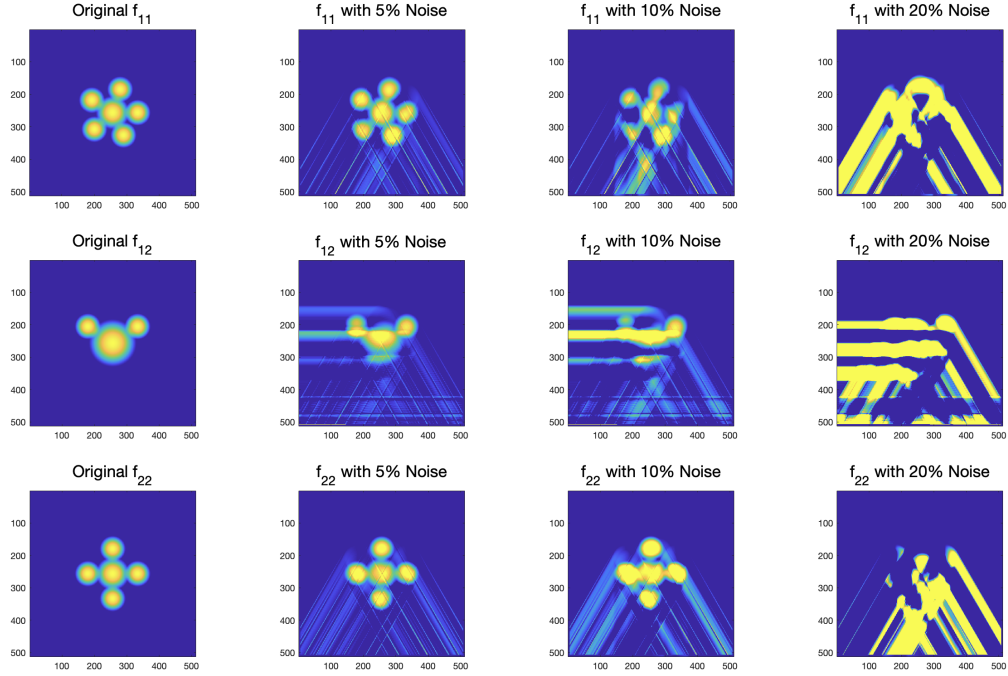


Figure 22: Reconstruction of f from $\mathcal{L}f, \mathcal{L}^1 f, \mathcal{T}f$ when $\mathbf{u} = (\cos \pi/3, \sin \pi/3)$ with 5%, 10% and 20% noise.

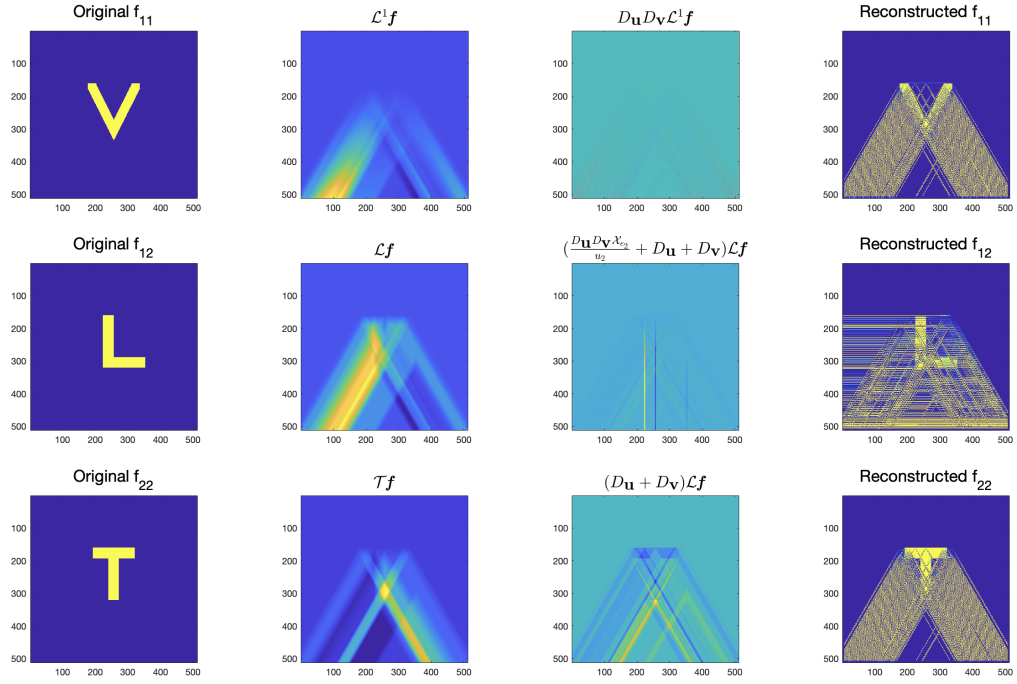


Figure 23: Reconstruction of f from $\mathcal{L}f, \mathcal{L}^1 f, \mathcal{T}f$, $\mathbf{u} = (\cos \pi/3, \sin \pi/3)$ using formulas (44), (43), (45).

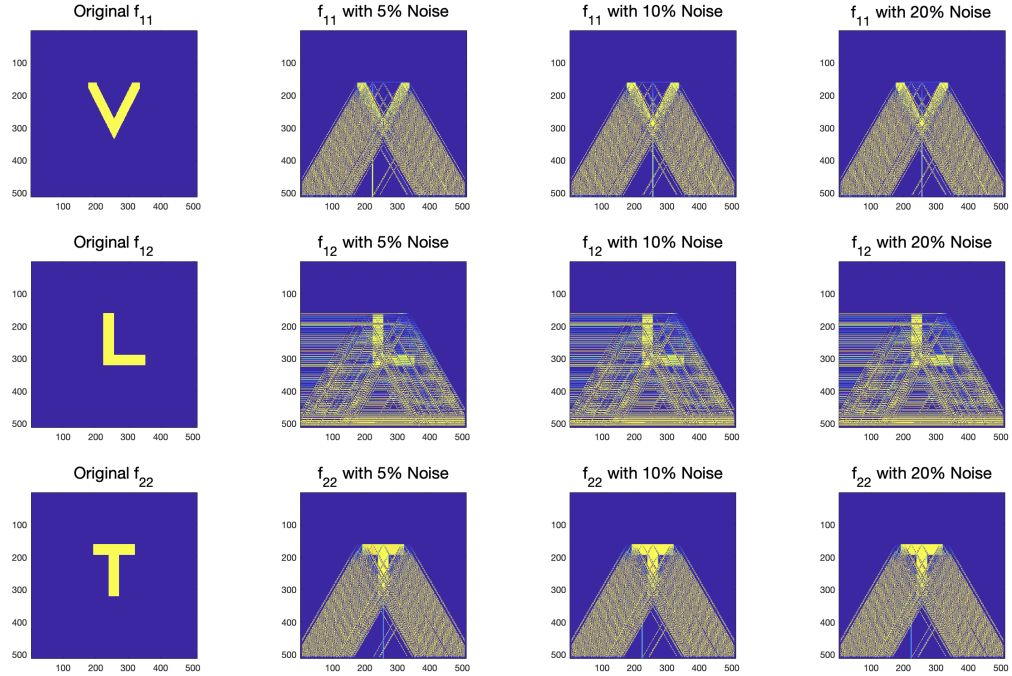


Figure 24: Reconstruction of f from $\mathcal{L}f, \mathcal{L}^1 f, \mathcal{T}f$ when $\mathbf{u} = (\cos \pi/3, \sin \pi/3)$ with 5%, 10% and 20% noise.

\mathbf{f}	No noise	5% Noise	10% Noise	20% Noise
f_{11}	13.77%	17.29%	61.49%	428.98%
f_{12}	806.32%	833.58%	990.84%	2404.38%
f_{22}	14.10%	18.43%	63.49%	445.50%

Table 12: Relative errors of reconstructing Phantom 1 from $\mathcal{L}\mathbf{f}, \mathcal{L}^1\mathbf{f}, \mathcal{T}\mathbf{f}, \mathbf{u} = (\cos \pi/3, \sin \pi/3)$.

\mathbf{f}	No noise	5% Noise	10% Noise	20% Noise
f_{11}	4009.19%	4036.22%	4215.82%	4218.84%
f_{12}	2408.93%	2422.88%	2534.95%	2532.71%
f_{22}	3041.98 %	3062.53%	3198.72%	3201.04%

Table 13: Relative errors of reconstructing Phantom 2 from $\mathcal{L}\mathbf{f}, \mathcal{L}^1\mathbf{f}, \mathcal{T}\mathbf{f}, \mathbf{u} = (\cos \pi/3, \sin \pi/3)$.

The inversion algorithms using the first moment transforms are highly ill-conditioned. The primary source of instability of the associated inversion formulas lies in the presence of an additional differentiation in the terms involving the first moment (e.g. see formulas (43)-(48)). As a result, the reconstructions based on these approaches have strong artifacts, which become worse when applied to non-smooth phantoms (compare Figures 21, 22 with Figures 23, 24). The situation is more severe in the setups where the V-lines have an opening angle far from $\pi/2$ (compare Figures 21-24 with Figures 25-28).

Although visually the patterns of the artifacts in Figure 24 do not seem to change much with the addition of noise to the data, the strengths of the artifacts change, which can be noticed from Table 13 of relative errors.

A similar phenomenon, related to the ill-conditioned inversions involving first moment VLTs due to the extra derivatives, was observed in the study of VLTs defined on vector fields in \mathbb{R}^2 (see [7]).

Next, we consider the recovery of \mathbf{f} from the combination $\mathcal{L}\mathbf{f}, \mathcal{L}^1\mathbf{f}$ and $\mathcal{M}\mathbf{f}$. In Figures 25 and 27, we use the inversion formulas (46), (47), and (48) to generate $f_{12}, f_{11},$ and f_{22} respectively for the smooth and non-smooth phantoms. Figures 26 and 28 show the reconstructions after adding different levels of noise for smooth and non-smooth phantoms, respectively.

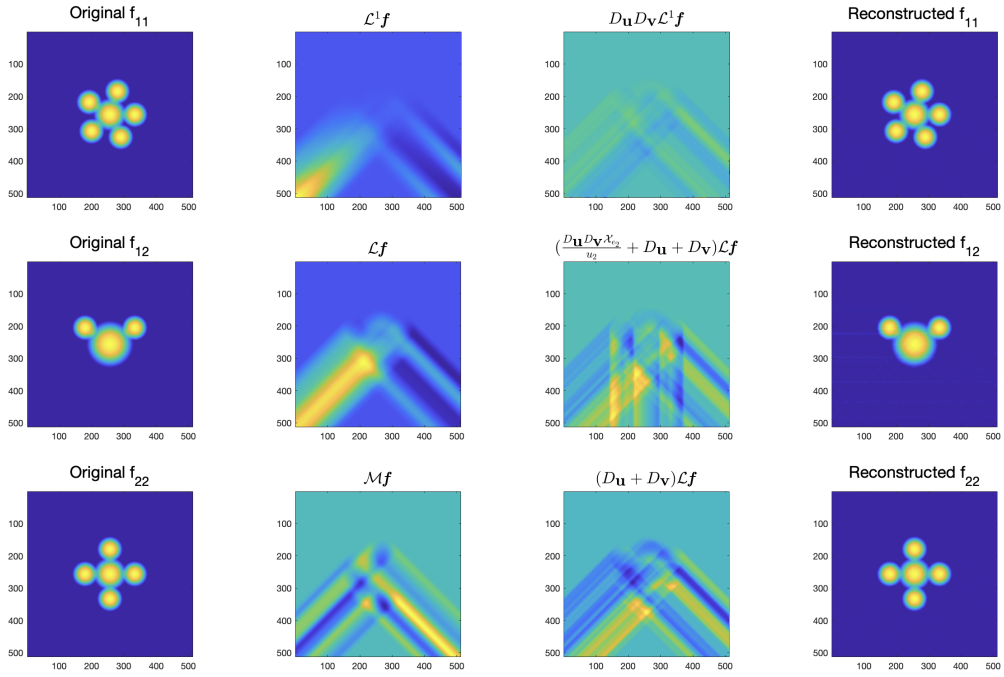


Figure 25: Reconstruction of f from $\mathcal{L}f, \mathcal{L}^1f, \mathcal{M}f, \mathbf{u} = (\cos \pi/4, \sin \pi/4)$ using formulas (46), (47), (48).

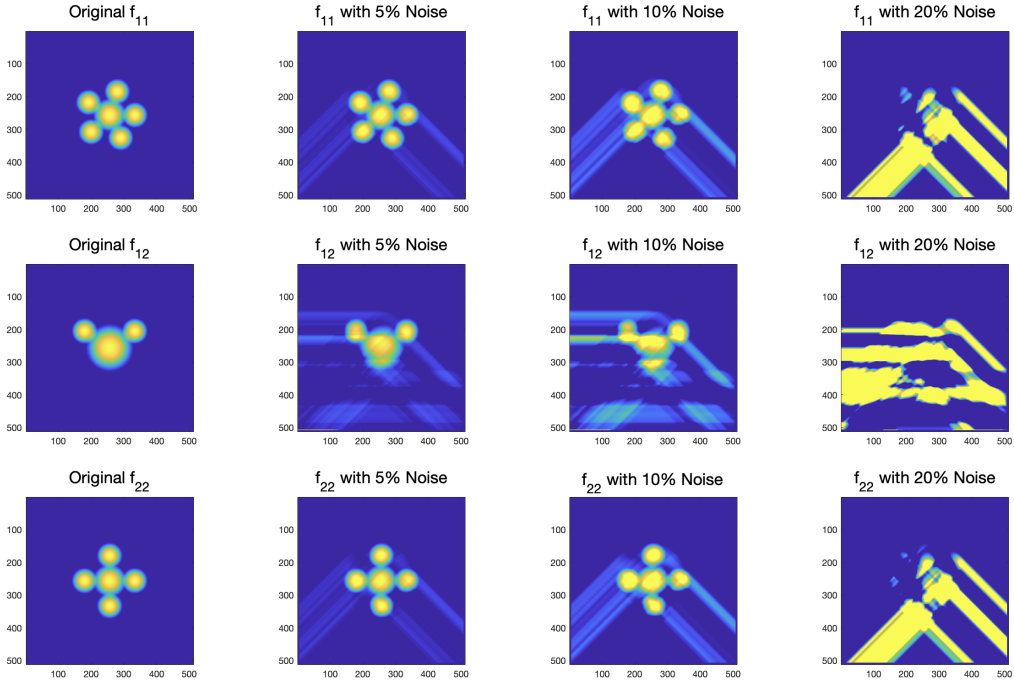


Figure 26: Reconstruction of f from $\mathcal{L}f, \mathcal{L}^1f, \mathcal{M}f, \mathbf{u} = (\cos \pi/4, \sin \pi/4)$ with 5%, 10% and 20% noise.

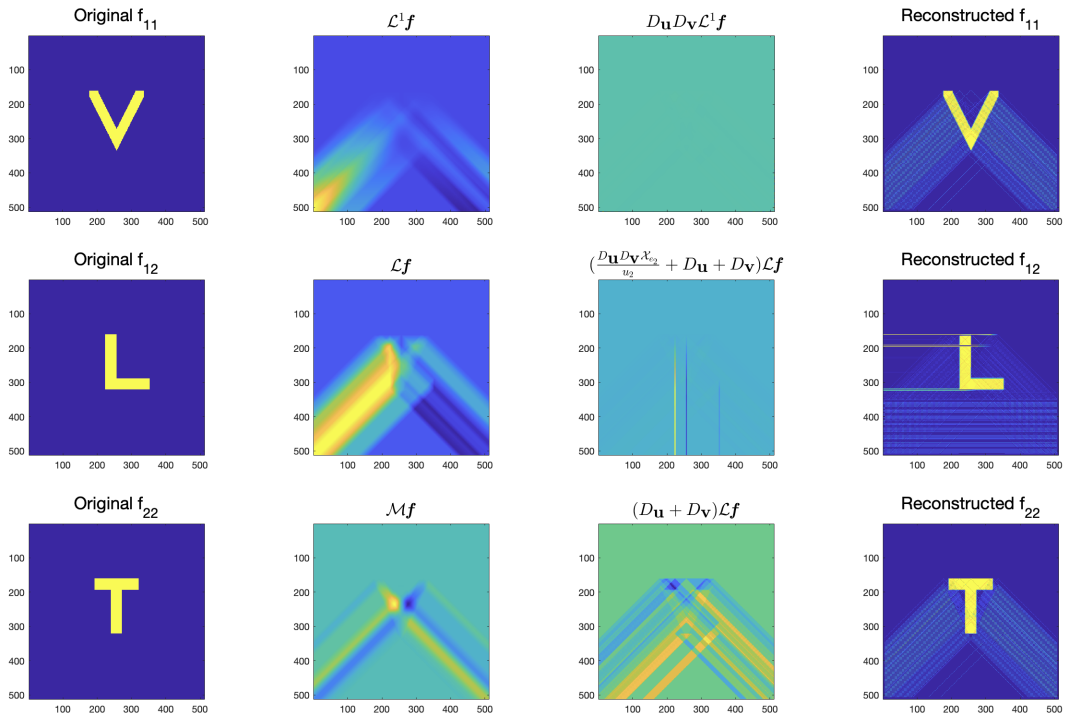


Figure 27: Reconstructions of f from $\mathcal{L}f, \mathcal{L}^1f, \mathcal{M}f$, $\mathbf{u} = (\cos \pi/4, \sin \pi/4)$, using formulas (46), (47), (48).

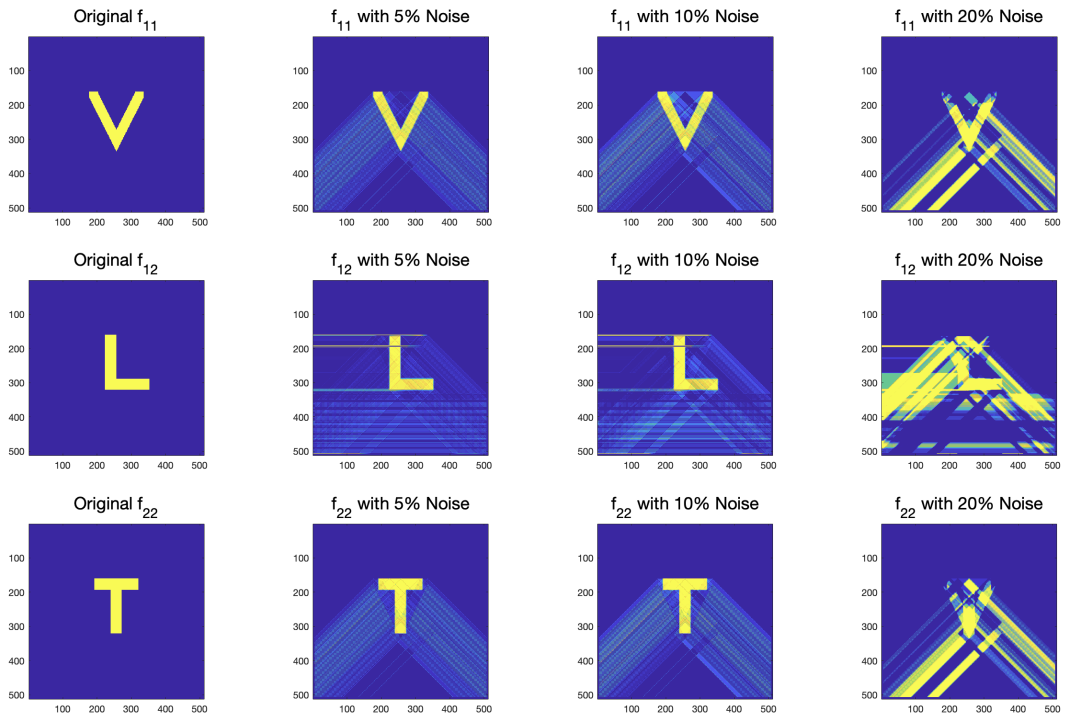


Figure 28: Reconstructions from $\mathcal{L}f, \mathcal{L}^1f, \mathcal{M}f$, $\mathbf{u} = (\cos \pi/4, \sin \pi/4)$, 5%, 10% and 20% noise.

\mathbf{f}	No noise	5% Noise	10% Noise	20% Noise
f_{11}	0.68%	11.72%	37.44%	273.99%
f_{12}	803.03%	840.92%	1008.68%	1325.82%
f_{22}	0.70%	11.70%	38.17%	278.72%

Table 14: Relative errors of reconstructing Phantom 1 from $\mathcal{L}\mathbf{f}, \mathcal{L}^1\mathbf{f}, \mathcal{M}\mathbf{f}, \mathbf{u} = (\cos \pi/4, \sin \pi/4)$.

\mathbf{f}	No noise	5% Noise	10% Noise	20% Noise
f_{11}	81.83%	82.69%	92.73%	204.12%
f_{12}	857.81%	883.65%	1026.22%	1378.59%
f_{22}	62.14%	62.80%	70.42%	156.51%

Table 15: Relative errors of reconstructing Phantom 2 from $\mathcal{L}\mathbf{f}, \mathcal{L}^1\mathbf{f}, \mathcal{M}\mathbf{f}, \mathbf{u} = (\cos \pi/4, \sin \pi/4)$.

4.4 Numerical implementation of inverting the tensor star transform

Before starting our discussion about the star transform of symmetric 2-tensor fields, let us quickly recall the definition of the star transform. Assume $\mathbf{f} \in C_c^2(S^2; \mathbb{R}^2)$, and let $\boldsymbol{\gamma}_1, \boldsymbol{\gamma}_2, \dots, \boldsymbol{\gamma}_m$ be distinct unit vectors in \mathbb{R}^2 . The star transform of \mathbf{f} is defined as

$$\mathcal{S}\mathbf{f} = \sum_{i=1}^m c_i \mathcal{X}_{\boldsymbol{\gamma}_i} \begin{bmatrix} \mathbf{f} \cdot \boldsymbol{\gamma}_i^2 \\ \mathbf{f} \cdot \boldsymbol{\gamma}_i \odot \boldsymbol{\gamma}_i^\perp \\ \mathbf{f} \cdot (\boldsymbol{\gamma}_i^\perp)^2 \end{bmatrix},$$

where c_1, c_2, \dots, c_m are non-zero constants in \mathbb{R} .

Definition 5. Consider the star transform $\mathcal{S}\mathbf{f}$ of a symmetric 2-tensor field \mathbf{f} with branches along directions $\boldsymbol{\gamma}_1, \boldsymbol{\gamma}_2, \dots, \boldsymbol{\gamma}_m$. We call

$$\mathcal{Z}_1 = \cup_{i=1}^m \{\boldsymbol{\xi} : \boldsymbol{\xi} \cdot \boldsymbol{\gamma}_i = 0\}$$

the set of singular directions of type 1 for \mathcal{S} .

Now, let us define three vectors in \mathbb{R}^3 , which will be important for further calculations. For $\boldsymbol{\xi} \in \mathbb{S}^1 \setminus \mathcal{Z}_1$, we define

$$\boldsymbol{\gamma}(\boldsymbol{\xi}) = - \sum_{i=1}^m \frac{c_i \boldsymbol{\gamma}_i^2}{\boldsymbol{\xi} \cdot \boldsymbol{\gamma}_i}, \quad \boldsymbol{\gamma}^\dagger(\boldsymbol{\xi}) = - \sum_{i=1}^m \frac{c_i \boldsymbol{\gamma}_i \odot \boldsymbol{\gamma}_i^\perp}{\boldsymbol{\xi} \cdot \boldsymbol{\gamma}_i}, \quad \boldsymbol{\gamma}^\perp(\boldsymbol{\xi}) = - \sum_{i=1}^m \frac{c_i (\boldsymbol{\gamma}_i^\perp)^2}{\boldsymbol{\xi} \cdot \boldsymbol{\gamma}_i}. \quad (49)$$

Definition 6. We call

$$\mathcal{Z}_2 = \left\{ \boldsymbol{\xi} : \boldsymbol{\gamma}^\dagger(\boldsymbol{\xi}) = 0 \right\} \cup \left\{ \boldsymbol{\xi} : \sum_{i=1}^m \frac{c_i}{\boldsymbol{\xi} \cdot \boldsymbol{\gamma}_i} = 0 \right\}$$

the set of singular directions of type 2 for \mathcal{S} .

Theorem 6. Let $\mathbf{f} \in C_c^2(S^2; D_1)$, and $\boldsymbol{\gamma}_1, \boldsymbol{\gamma}_2, \dots, \boldsymbol{\gamma}_m$ be the branch directions of the star transform. Let

$$\mathcal{Q}(\boldsymbol{\xi}) = \begin{bmatrix} \boldsymbol{\gamma}(\boldsymbol{\xi}) \\ \boldsymbol{\gamma}^\dagger(\boldsymbol{\xi}) \\ \boldsymbol{\gamma}^\perp(\boldsymbol{\xi}) \end{bmatrix}.$$

Then for any $\boldsymbol{\xi} \in \mathbb{S}^1 \setminus (\mathcal{Z}_1 \cup \mathcal{Z}_2)$ and any $s \in \mathbb{R}$ we have

$$[\mathcal{Q}(\boldsymbol{\xi})]^{-1} \frac{d}{ds} \mathcal{R}(\mathcal{S}\mathbf{f})(\boldsymbol{\xi}, s) = \mathcal{R}\mathbf{f}(\boldsymbol{\xi}, s) \quad (50)$$

where $\mathcal{R}\mathbf{f}$ is the component-wise Radon transform of \mathbf{f} .

To reconstruct numerically the tensor from its star transform, we consider a star with the branches along $\boldsymbol{\gamma}_i = (\cos \phi_i, \sin \phi_i)$, where $\phi_1 = 0, \phi_2 = 2\pi/3, \phi_3 = 4\pi/3$, and weights $c_i = 1$ for $i = 1, 2, 3$. It can be easily verified that in this case $\mathcal{Z}_2 = \emptyset$ and \mathcal{Z}_1 consists of six directions. Therefore, formula (50) will recover $\mathcal{R}\mathbf{f}(\boldsymbol{\xi}, s)$ for all but six $\boldsymbol{\xi} \in \mathbb{S}^1$, allowing the recovery of \mathbf{f} using any standard inversion technique for the (classical) Radon transform.

The numerical reconstruction is performed using the following steps:

- We calculate $\mathcal{X}_{\boldsymbol{\gamma}_i}(\mathbf{f} \cdot \boldsymbol{\gamma}_i^2), \mathcal{X}_{\boldsymbol{\gamma}_i}(\mathbf{f} \cdot \boldsymbol{\gamma}_i \odot \boldsymbol{\gamma}_i^\perp), \mathcal{X}_{\boldsymbol{\gamma}_i}(\mathbf{f} \cdot (\boldsymbol{\gamma}_i^\perp)^2)$. Then, combining these according to the definition, we compute the (forward) data corresponding to $\mathcal{S}\mathbf{f}$.
- Using the Matlab function **radon**, we generate the data for $\mathcal{R}(\mathcal{S}\mathbf{f})(\boldsymbol{\xi}, s)$ and then calculate $\frac{d}{ds} \mathcal{R}(\mathcal{S}\mathbf{f})(\boldsymbol{\xi}, s)$.
- Next, for each value of $\boldsymbol{\xi}$ we compute $[\mathcal{Q}(\boldsymbol{\xi})]^{-1}$ and multiply it with $\frac{d}{ds} \mathcal{R}(\mathcal{S}\mathbf{f})(\boldsymbol{\xi}, s)$.
- Finally, using **iradon** to $[\mathcal{Q}(\boldsymbol{\xi})]^{-1} \frac{d}{ds} \mathcal{R}(\mathcal{S}\mathbf{f})(\boldsymbol{\xi}, s)$, we recover \mathbf{f} .

In Figure 29, we show the reconstruction using the algorithm discussed above for the non-smooth phantom. Figure 30 demonstrates the results of the reconstruction in the presence of noise. The relative errors of the reconstructions are summarized in Table 16.

The artifacts present in the reconstructions using the star transform are due to the cutting of the data on the edges of the image domain. Notice, that almost all of those artifacts are located outside of the field of view, i.e. the a priori known disc of support of the phantoms. Therefore, one can eliminate those artifacts through image post-processing, by assigning the value of zero to all pixels outside of that disc. In that case, the relative errors presented in Table 16 will also substantially decrease.

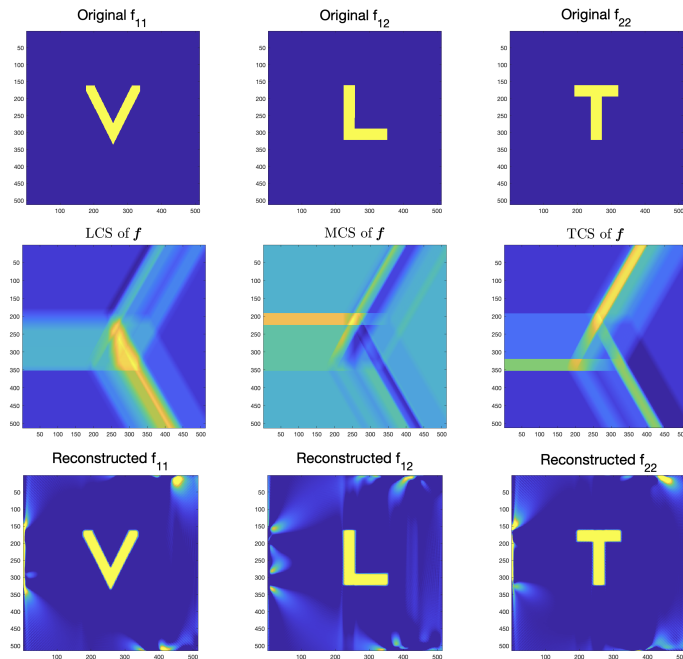


Figure 29: Row 1: components of \mathbf{f} ; Row 2: longitudinal (LCS), mixed(MCS), and transverse (TCS) components of $\mathcal{S}\mathbf{f}$; Row 3: reconstructed components of \mathbf{f} using formula (50).

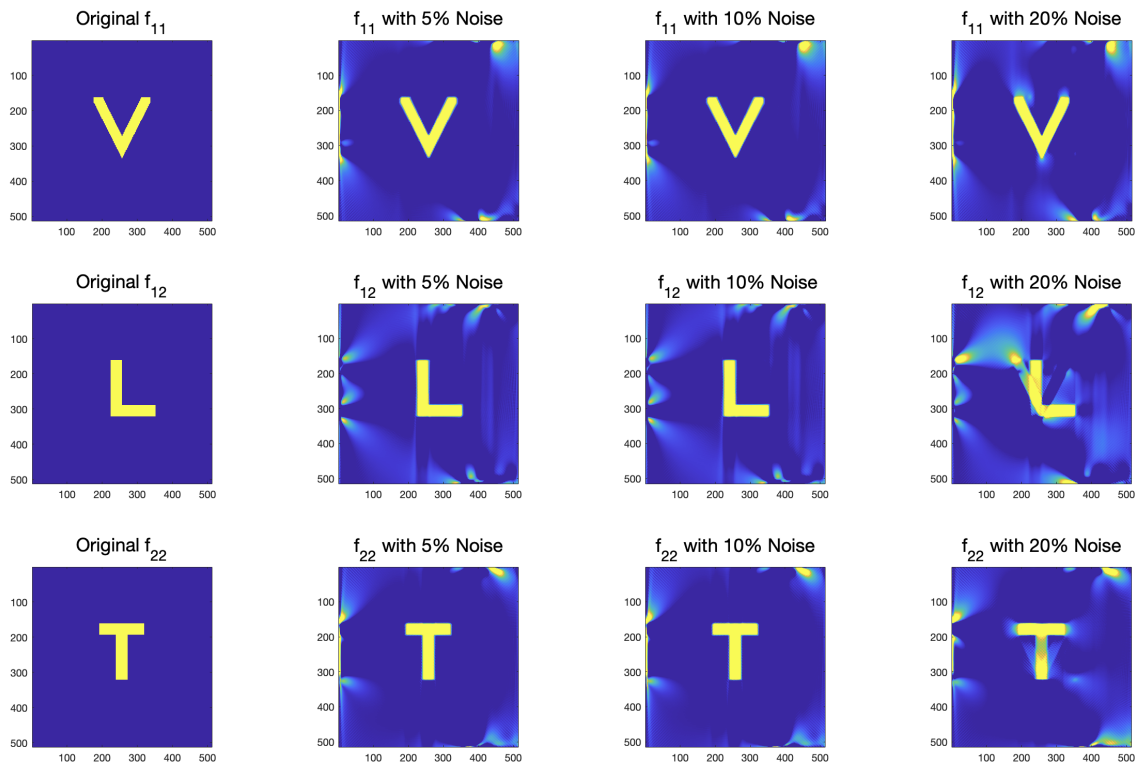


Figure 30: Reconstruction of \mathbf{f} from $\mathcal{S}\mathbf{f}$ with 5%, 10% and 20% noise

\mathbf{f}	No noise	5% Noise	10% Noise	20% Noise
f_{11}	114.01%	114.72%	128.88%	175.17%
f_{12}	92.41%	96.36%	96.81%	115.22%
f_{22}	95.56%	96.02%	109.25%	139.61%

Table 16: Relative errors of the reconstruction of \mathbf{f} from $\mathcal{S}\mathbf{f}$.

5 Acknowledgements

GA was partially supported by the NIH grant U01-EB029826. RM was partially supported by SERB SRG grant No. SRG/2022/000947. IZ was supported by the Prime Minister’s Research Fellowship from the Government of India.

References

- [1] Gaik Ambartsoumian. Inversion of the V-line Radon transform in a disc and its applications in imaging. *Computers & Mathematics with Applications*, 64(3):260–265, 2012. [1](#), [2](#)
- [2] Gaik Ambartsoumian. V-line and conical Radon transforms with applications in imaging. In Ronny Ramlau and Otmar Scherzer, editors, *The Radon Transform: The First 100 Years and Beyond*, pages 143–168. De Gruyter, Berlin, Boston, 2019. [2](#)
- [3] Gaik Ambartsoumian. *Generalized Radon Transforms and Imaging by Scattered Particles: Broken Rays, Cones, and Stars in Tomography*. World Scientific, 2023. [1](#)
- [4] Gaik Ambartsoumian and Mohammad J. Latifi. The V-line transform with some generalizations and cone differentiation. *Inverse Problems*, 35(3):034003, 2019. [2](#)
- [5] Gaik Ambartsoumian and Mohammad J. Latifi. Inversion and symmetries of the star transform. *The Journal of Geometric Analysis*, 31(11):11270–11291, 2021. [2](#)
- [6] Gaik Ambartsoumian, Mohammad J. Latifi, and Rohit K. Mishra. Generalized V-line transforms in 2D vector tomography. *Inverse Problems*, 36(10):104002, 2020. [2](#)
- [7] Gaik Ambartsoumian, Mohammad J. Latifi, and Rohit K. Mishra. Numerical implementation of generalized V-line transforms on 2D vector fields and their inversions. *SIAM Journal on Imaging Sciences*, 17(1):595–631, 2024. [2](#), [7](#), [25](#), [28](#)
- [8] Gaik Ambartsoumian, Rohit K. Mishra, and Indrani Zamindar. V-line 2-tensor tomography in the plane. *Inverse Problems*, 40(3):035003, 2024. [1](#), [2](#), [3](#), [5](#), [6](#), [8](#), [9](#), [10](#), [11](#), [13](#), [14](#)
- [9] Gaik Ambartsoumian and Sunghwan Moon. A series formula for inversion of the V-line Radon transform in a disc. *Computers & Mathematics with Applications*, 66(9):1567–1572, 2013. [1](#), [2](#)
- [10] Gaik Ambartsoumian and Sarah K. Patch. Thermoacoustic tomography: numerical results. In *Photons Plus Ultrasound: Imaging and Sensing 2007: The Eighth Conference on Biomedical Thermoacoustics, Optoacoustics, and Acousto-optics*, volume 6437, pages 346–355. SPIE, 2007. [23](#)

- [11] Gaik Ambartsoumian and Souvik Roy. Numerical inversion of a broken ray transform arising in single scattering optical tomography. *IEEE Transactions on Computational Imaging*, 2(2):166–173, 2016. [1](#)
- [12] Roman Basko, Gengsheng L. Zeng, and Grant T. Gullberg. Analytical reconstruction formula for one-dimensional Compton camera. *IEEE Transactions on Nuclear Science*, 44(3):1342–1346, Jun 1997. [1](#)
- [13] Roman Basko, Gengsheng L. Zeng, and Grant T. Gullberg. Fully three dimensional image reconstruction from “V”-projections acquired by Compton camera with three vertex electronic collimation. In *1997 IEEE Nuclear Science Symposium Conference Record*, volume 2, pages 1077–1081, Nov 1997. [1](#)
- [14] Rahul Bhardwaj, Rohit K. Mishra, and Manmohan Vashisth. Inversion of generalized V-line transforms of vector fields in \mathbb{R}^2 . *Preprint, arXiv:2404.12479*, 2024. [2](#)
- [15] Evgeny Yu. Derevtsov and Ivan E. Svetov. Tomography of tensor fields in the plane. *Eurasian Journal of Mathematical and Computer Applications*, 3(2):24–68, 2015. [3](#), [11](#)
- [16] Dale R. Durran. *Numerical Methods For Wave Equations In Geophysical Fluid Dynamics*, volume 32. Springer Science & Business Media, 2013. [10](#)
- [17] Lucia Florescu, Vadim A. Markel, and John C. Schotland. Single-scattering optical tomography: Simultaneous reconstruction of scattering and absorption. *Physical Review E*, 81:016602, Jan 2010. [1](#)
- [18] Lucia Florescu, Vadim A. Markel, and John C. Schotland. Inversion formulas for the broken-ray Radon transform. *Inverse Problems*, 27(2):025002, 2011. [2](#)
- [19] Lucia Florescu, Vadim A. Markel, and John C. Schotland. Nonreciprocal broken ray transforms with applications to fluorescence imaging. *Inverse Problems*, 34(9):094002, 2018. [1](#)
- [20] Lucia Florescu, John C. Schotland, and Vadim A. Markel. Single-scattering optical tomography. *Physical Review E*, 79:036607, Mar 2009. [1](#)
- [21] Rim Gouia-Zarrad. Analytical reconstruction formula for n -dimensional conical Radon transform. *Computers & Mathematics with Applications*, 68(9):1016–1023, 2014. [2](#)
- [22] Rim Gouia-Zarrad and Gaik Ambartsoumian. Exact inversion of the conical Radon transform with a fixed opening angle. *Inverse Problems*, 30(4):045007, 2014. [2](#)
- [23] Gabor T Herman. *Fundamentals of Computerized Tomography: Image Reconstruction From Projections*. Springer Science & Business Media, 2009. [23](#)
- [24] Joonas Ilmavirta and Gabriel P. Paternain. Broken ray tensor tomography with one reflecting obstacle. *Communications in Analysis and Geometry*, 30(6):1269–1300, 2022. [2](#)
- [25] Joonas Ilmavirta and Mikko Salo. Broken ray transform on a Riemann surface with a convex obstacle. *Communications in Analysis and Geometry*, 24(2):379–408, 2016. [2](#)
- [26] Shubham R. Jathar, Manas Kar, and Jesse Railo. Broken ray transform for twisted geodesics on surfaces with a reflecting obstacle. *The Journal of Geometric Analysis*, 34(7):212, 2024. [2](#)

- [27] Alexander Katsevich and Roman Krylov. Broken ray transform: inversion and a range condition. *Inverse Problems*, 29(7):075008, 2013. [2](#)
- [28] Roman Krylov and Alexander Katsevich. Inversion of the broken ray transform in the case of energy-dependent attenuation. *Physics in Medicine & Biology*, 60(11):4313, 2015. [1](#), [2](#)
- [29] Marcela Morvidone, Mai K. Nguyen, Tuong T. Truong, and Habib Zaidi. On the V-line Radon transform and its imaging applications. *International Journal of Biomedical Imaging*, 2010:208179, 2010. [1](#)
- [30] Victor Palamodov. Reconstruction from cone integral transforms. *Inverse Problems*, 33(10):104001, 2017. [2](#)
- [31] Gaël Rigaud, Rémi Régnier, Mai K. Nguyen, and Habib Zaidi. Combined modalities of Compton scattering tomography. *IEEE Transactions on Nuclear Science*, 60(3):1570–1577, 2013. [1](#)
- [32] Vladimir A. Sharafutdinov. *Integral Geometry of Tensor Fields*. De Gruyter, Berlin, New York, 1994. [3](#)
- [33] Brian Sherson. *Some Results in Single-Scattering Tomography*. PhD thesis, Oregon State University, 2015. PhD Advisor: D. Finch. [1](#), [2](#)
- [34] Tuong T. Truong and Mai K. Nguyen. On new V-line Radon transforms in \mathbb{R}^2 and their inversion. *Journal of Physics A: Mathematical and Theoretical*, 44(7):075206, jan 2011. [1](#)
- [35] Michael R Walker and Joseph A. O’Sullivan. Iterative algorithms for joint scatter and attenuation estimation from broken ray transform data. *IEEE Transactions on Computational Imaging*, 7:361–374, 2021. [1](#)
- [36] Fan Zhao, John C. Schotland, and Vadim A. Markel. Inversion of the star transform. *Inverse Problems*, 30(10):105001, 2014. [2](#)